

Naval Research Laboratory

Stennis Space Center, MS 39529-5004



NRL/MR/7332--98-8216

Technical Evaluation of Constructing Wind and Wave Climatologies Using Spaceborne Altimeter Output with a Demonstration Study in the Yellow and East China Seas

Prepared for:

The U.S. Naval Oceanographic Office, Stennis Space Center, MS 39522
Contract No. N6230698WR80110
and

The U.S. Army Corps of Engineers Coastal and Hydraulic Laboratory
Vicksburg, MS 39180
Contract No. W81EWF81381320

PAUL A. HWANG

WILLIAM J. TEAGUE

Ocean Sciences Branch
Oceanography Division

November 10, 1998

Approved for public release; distribution is unlimited.

19990105 000

REPORT DOCUMENTATION PAGE

Form Approved
OMB No. 0704-0188

Public reporting burden for this collection of information is estimated to average 1 hour per response, including the time for reviewing instructions, searching existing data sources, gathering and maintaining the data needed, and completing and reviewing the collection of information. Send comments regarding this burden or any other aspect of this collection of information, including suggestions for reducing this burden, to Washington Headquarters Services, Directorate for Information Operations and Reports, 1215 Jefferson Davis Highway, Suite 1204, Arlington, VA 22202-4302, and to the Office of Management and Budget, Paperwork Reduction Project (0704-0188), Washington, DC 20503.

1. AGENCY USE ONLY (Leave blank)	2. REPORT DATE	3. REPORT TYPE AND DATES COVERED	
	November 10, 1998	Final	
4. TITLE AND SUBTITLE		5. FUNDING NUMBERS	
Technical Evaluation of Constructing Wind and Wave Climatologies Using Spaceborne Altimeter Output with a Demonstration Study in the Yellow and East China Seas		Job Order No. 73-6805-09 Program Element No. Project No. N6230698WR80110 & Task No. W81EWF81381320 Accession No.	
6. AUTHOR(S)			
Paul A. Hwang and William J. Teague			
7. PERFORMING ORGANIZATION NAME(S) AND ADDRESS(ES)		8. PERFORMING ORGANIZATION REPORT NUMBER	
Naval Research Laboratory Oceanography Division Stennis Space Center, MS 39529-5004		NRL/MR/7332--98-8216	
9. SPONSORING/MONITORING AGENCY NAME(S) AND ADDRESS(ES)		10. SPONSORING/MONITORING AGENCY REPORT NUMBER	
Naval Oceanographic Office Stennis Space Center, MS 39522-5001		U.S. Army Corps of Engineers Coastal and Hydraulic Laboratory Vicksburg, MS 39180-6199	
11. SUPPLEMENTARY NOTES			
12a. DISTRIBUTION/AVAILABILITY STATEMENT		12b. DISTRIBUTION CODE	
Approved for public release; distribution unlimited.			
13. ABSTRACT (Maximum 200 words)			
<p>The density of data output from spaceborne altimeters is an impressive 7-km alongtrack. This is an excellent data source to the study of global and regional wind and wave conditions. A technical evaluation of constructing regional climatologies of winds and waves is presented. The accuracy of the measurements is summarized from several earlier comparison studies. The results indicate that the wind speeds and wave heights measured by satellite altimeters are of outstanding quality. For the construction of a regional climatology, the spatial resolution (grid size) and temporal resolution (time bin) are important considerations. Our analysis indicates that from a single satellite seasonal statistics with 1° resolution can be achieved. With combined satellite output, monthly climatologies with 0.25° resolution is possible.</p> <p>A demonstration study is presented for the region of Yellow and East China Seas using the TOPEX output. The results show significant temporal and spatial structure of the wind and wave distributions in the region. Four distinct domains of winds and waves can be defined for the area defined by (115° E, 20° N) and (130° E, 42° N): the Yellow Sea, the East China Sea, the Kuroshio, and South of Ryukyu Islands. The distinction of each area is outlined.</p>			
14. SUBJECT TERMS		15. NUMBER OF PAGES	
spaceborne altimeter, wind, wave, climatology		40	
		16. PRICE CODE	
17. SECURITY CLASSIFICATION OF REPORT	18. SECURITY CLASSIFICATION OF THIS PAGE	19. SECURITY CLASSIFICATION OF ABSTRACT	20. LIMITATION OF ABSTRACT
Unclassified	Unclassified	Unclassified	SAR

Table of Contents

Table of Contents	i
Abstract	1
1. Introduction	1
2. Altimeter measurement of winds and waves.....	1
2.1. Principle of measurement.....	1
2.2. Validation with in situ buoy data.....	2
2.3. Sea, swell and directional information	2
3. Regional and global climatology.....	4
3.1. Spatial and temporal resolution.....	4
3.2. Seasonal and annual climatology in the Yellow and East China Seas	6
3.3. Modification of winds and waves by the Kuroshio	7
3.4. Domains of winds and waves in the Yellow and East China Seas	8
4. Additional issues	9
4.1. Land proximity	9
4.2. Combining multiple satellite measurements -- cross calibration.....	10
5. Summary and conclusions.....	10
Acknowledgment.....	11
Appendix I. Comparison of altimeter and buoy measurements of wind speed and wave height.....	11
A. Significant wave height	11
B. Wind speed	12
C. Wave period.....	13
References	15
List of tables	17
List of figures	18

Technical Evaluation of Constructing Wind and Wave Climatologies Using Spaceborne Altimeter Output

with a demonstration study in the Yellow and East China Seas

1. Introduction

Knowledge of wave and meteorological conditions in coastal regions is important for mission planning and on-scene decision for Mine Warfare, Amphibious, and Special Warfare operations. These three communities require information on a variety of environmental parameters such as wave/swell, wind speed and direction.

Remote sensing from space provides a synoptic view of the ocean wind and wave fields. For example, wind speed and significant wave height are standard outputs of spaceborne altimeters such as TOPEX/POSEIDON (hereafter referred to as TOPEX for brevity). Comparisons of the altimeter measured wind speed and wave height with surface buoy data have shown very positive agreement (e.g., Carter et al., 1992; Cotton and Carter, 1994; Ebuchi and Kawamura, 1994; Freilich and Challenor, 1994; Gower, 1996; Hwang et al., 1998a). With an along-track resolution of 7 km, the spaceborne measurement represents a valuable data source for the study of regional oceanography. This report will evaluate the application of the spaceborne altimeter data set for the construction of regional wind and wave climatologies. Section 2 presents a brief discussion of altimeter wind and wave measurement, and a summary of altimeter data validation with in situ buoy data. Error estimates and statistical measures of wind speeds and significant wave heights are provided. Feasibility of deriving sea and swell information, as well as directional information will be discussed. Section 3 presents a resolution analysis (grid size and time bin) for single and multiple satellite combinations. Also a demonstration study is given on developing regional climatologies using TOPEX altimeter data in the Yellow and East China Seas. The spatial grid size of 1° , and temporal averaging bin size of 3 months are used for this single satellite analysis. The results illustrate important features in the seasonal variation and spatial pattern of winds and waves in the region. For even higher spatial and temporal resolution, the data density can be increased by various combinations of TOPEX, ERS and Geosat Follow-On (GFO). Section 4 discusses the issues of proximity to coastline, and performance differences of several altimeters (Cotton and Carter, 1994; Cotton, 1998). A summary of the study is presented in Section 5.

2. Altimeter measurement of winds and waves

2.1. Principle of measurement

The wave height from a spaceborne altimeter is determined from the distortion of the reflected radar wave from the ocean surface. As illustrated in **Figure 1**. If the surface is flat (**Figure 1a**), the reflected wave form is a mirror image of the incident wave. Roughness on the surface will cause the incident wave to reflect back earlier in time from the crest region and later from the troughs, as shown in **Figures 1b** and **1c**. The wave form is distorted and deviates from the original incident waveform. The degree of distortion is proportional to the characteristic height of the surface roughness. The altimeter typically sends out a large number of pulses (for TOPEX, it is 4000 pulses/s). The wave height derived from the wave form distortion represents an ensemble average from a large number of measurements.

Derivation of wind speed from microwave radars is based on the correlation of surface roughness and radar backscattering intensity (the normalized radar backscatter cross section, σ_0). For the spaceborne altimeters, specular reflection is the primary mechanism of radar backscatter. In this mode, roughness on the surface causes incident radar waves to diffuse and scatter away from the aperture of radar reception, and the smoother the surface the higher the backscatter. On the ocean surface, short ocean waves are the primary contributors to the surface roughness. Because these short water waves are mainly wind generated, a higher σ_0 corresponds to a lower wind speed and vice versa.

A large volume of literature is available on the subject of altimeter technology and the interpretation of the waveform and radar cross sections. For more detailed information see, e.g., Chelton et al. (1994) and the references therein.

2.2. Validation with in situ buoy data

Extensive studies of altimeter measurements of wind and wave parameters have been published (e.g., Brown et al., 1981; Chelton and Wentz, 1986; Carter et al., 1992; Wu 1992; Cotton and Carter, 1994; Witter and Chelton, 1994; Freilich and Challenor, 1994; Ebuchi and Kawamura, 1994; Gower 1996; Hwang et al., 1998a; and the references therein). These studies have shown consistently that the significant wave height derived from the altimeter is essentially identical to that measured by ocean surface buoys. In particular, Gower (1996) presents a comprehensive comparison of wind speed and wave height between the TOPEX altimeter measurements (first 47 cycles, September 1992 to December 1993) and 14 moored buoys along the West Coast of Canada. Hwang et al. (1998a) compared 3.15 years TOPEX measurements (September 1992 to December 1995) with 5 NDBC (National Data Buoy Center) buoys in the Gulf of Mexico. Both studies show that when the distance between the buoy location and the satellite footprint is within 10 km, the rms difference of significant wave heights between the two data sets is less than 0.14 m. Ebuchi and Kawamura (1994) performed a comparison of TOPEX altimeter wind speeds and wave heights with three buoys around Japan using the first 30 cycles (about 10 months) of data. The comparison statistics from these three studies are summarized in Table 1.

The comparison statistics vary from data set to data set, and from study to study. As the data quantity increases, the statistics become more comparable. For the significant wave height, the bias is on the order of a few centimeters, the rms difference is approximately 0.14 m, the regression coefficient (that is, the slope of the scatter plot when the intercept is forced to zero, representing the proportionality factor between altimeter and buoy data) is between 0.97 to 1.0, and the correlation coefficient is 0.97. For wind speed, the bias is approximately 0.13 m/s, the rms difference is 1.3 m/s, the proportionality factor is between 0.98 to 1.12, and the correlation coefficient is 0.85. These statistics illustrate the high accuracy in the wind speed and wave height output from spaceborne altimeters.

Because wind speed, wave height and wave period are closely related, Hwang et al. (1998a) present an algorithm to obtain a characteristic wave period from the altimeter wind speed and wave height. The results are in excellent agreement with buoy measurements (Table 1C). **Figure 2** shows an example of TOPEX measured wave heights, wave speeds, and wave periods compared with buoy data. The measurements from the two systems are essentially equivalent. The average ratio with one standard deviation of the wave heights, wind speeds, and characteristic wave periods are 1.01 ± 0.14 , 1.05 ± 0.28 , 1.06 ± 0.13 , respectively. The distributions of these ratios are shown in **Figures 2d-f**, illustrating very narrow spreading. More detailed discussions can be found in the original studies (e.g., Ebuchi and Kawamura, 1994; Gower, 1996; Hwang et al., 1998a). An except of Hwang et al (1998a) is given in Appendix I.

2.3. Sea, swell and directional information

Ocean waves can be divided into two major categories in terms of generation processes: sea and swell. Sea is the locally generated wind waves, and swell is long waves propagated over a long distance, and is typically generated from distant storms. Sea is characterized by its chopping appearance, broad band width, and confused directional distribution. The correlation of wave height and wave period with wind speed is quantifiable in a growing sea condition (e.g., Hasselmann et al., 1973, 1976; Toba, 1978, 1997; Donelan, 1990). Swell, on the other hand, is well sorted due to the large propagation distance. Following the dispersion relationship of the ocean surface gravity waves, water waves of longer periods travel faster than those with shorter periods. The swell waveform is typically smooth and almost sinusoidal. Because of its distant generation source, the wave height and wave period are not correlated to local wind condition. Since spaceborne altimeters provide output of wave height and wind speed simultaneously, some information on sea and swell may be derived from our understanding of wind wave generation. However, because wave period is not available, the information is incomplete and some

judgement is needed to extracting this information from altimeter output. One possible approach to distinguish swell and sea conditions from satellite altimeter data is outlined below.

Under the condition of active wind wave generation the close correlation of wave height, wind speed and wave period has been recognized. For example, Hwang et al. (1998a) describe two formulas established on theoretical consideration and empirical verification:

$$\frac{U_{10}}{gT_p} = 4.8 \times 10^{-2} \left(\frac{U_{10}^2}{gH_s} \right)^{2/3} \quad (1)$$

due to Hasselmann et al. (1973, 1976) and Toba (1978), and

$$\frac{U_{10}}{gT_a} = 6.0 \times 10^{-2} \left(\frac{U_{10}^2}{gH_s} \right)^{0.6} \quad (2)$$

due to empirical fitting of the Gulf of Mexico dataset. In these two equations, T_p represents the wave period of the peak spectral component, and T_a is the average wave period weighted by the spectral density $S(f)$, and is defined as

$$T_a = \left[\frac{\int f^2 S(f) df}{\int S(f) df} \right]^{-1/2} \quad (3)$$

The ratio of T_p/T_a is typically about 1.25. Empirically, the spectral peak period is related to wind speed by

$$T_p = \frac{2\pi U_{10}}{g} \quad (4)$$

Substituting (4) into (1) and (2), the dimensionless parameter (gH_s/U_{10}^2) derivable from altimeter output at saturation is

$$\frac{gH_s}{U_{10}^2} = 0.165, \quad (5)$$

based on (1), and is

$$\frac{gH_s}{U_{10}^2} = 0.134, \quad (6)$$

based on (2). The discrepancy between the two "constants" is approximately 20%, which is within typical uncertainties of oceanographic data. From experience, allowing a factor of two as the envelope of oceanographic data scatter, it is recommended that

$$\frac{gH_s}{U_{10}^2} > 0.3 \quad (7)$$

be used for discriminating sea and swell conditions. Further quantification of separating the swell and the wind sea components can be achieved from energy conservation, expressed as

$$H_s^2 = H_{sea}^2 + H_{swell}^2, \quad (8)$$

with the wind sea component following (7), that is

$$H_{sea}^2 = 0.09 U_{10}^4 / g^2. \quad (9)$$

If $H_s^2 \leq H_{sea}^2$, the wave field is considered pure wind sea, for $H_s^2 > H_{sea}^2$, the swell component is obtained by

$$H_{swell}^2 = H_s^2 - H_{sea}^2, \quad (10)$$

or with the substitution of (9)

$$H_{swell}^2 = H_s^2 - 0.09 U^4 / g^2. \quad (11)$$

Figure 3 shows an example of this application. The scatter plot of H_s vs. U_{10} is shown in **Figure 3a**, with circles representing buoy data and crosses representing altimeter measurements. The solid curve is based on $gH_s/U_{10}^2 = 0.3$, serving as the upper limit of wind sea component of the wave height. The energy ratio of swell to sea is shown in **Figure 3b**. Symbols used are identical to those in **Figure 3a**. In general, swell conditions dominate in low wind cases, as one would expect. The results derived from altimeter data are similar to those from buoy measurements (**Figure 3c**).

Obtaining the directional information from satellite altimeter output has not been attempted before. One possibility is to take into consideration the spatial distribution from the along-track data sequence and combine with our understanding of wave growth due to wind generation or decay in shoaling processes. **Figure 4** shows examples of wind and wave distributions along a satellite track in the Yellow and East China Seas region for eight passes in 1994. The difference in the wind and wave trends along the track may contain some limited directional information. However, for each satellite pass, there is only one “cut” across the wind or wave field, and thus the directional information is not likely to be very good.

3. Regional and global climatology

The analysis presented in the last section demonstrates convincingly that the wind speed and wave height measured from a spaceborne altimeter are statistically equivalent to those measured by in situ ocean buoys in deep water and regions away from immediate land effects. One of the most important features of remote sensing is the capability of providing spatial measurements at a very high speed. The typical speed of the spacecraft is 7 km/s over the world, thus it scans one cycle of the earth in approximately 100 minutes. The high speed spatial coverage generates a valuable database of high density wind and wave measurements for constructing regional and global climatology. This section provides technical discussion on issues of spatial and temporal resolutions from single and multiple satellites. The sampling strategy and analysis approach for a climatology can then be established based on assessment of resolutions. Examples of seasonal and annual climatology for the Yellow and East China Seas derived from TOPEX data are illustrated. Several oceanographic features affecting wind and wave climatologies in this region are outlined.

3.1. Spatial and temporal resolution.

Ground tracks for TOPEX consist of 127 tracks, repeat every 9.92 days, and are separated by about 3 degrees of longitude. Geosat and Geosat Follow-On (referred to as GFO) ground tracks total 244, repeat every 17.05 days, and are separated by about 1.5 degrees of longitude. ERS 1 and 2 (referred to as ERS) are most densely spaced but have the poorest temporal coverage. Ground tracks for ERS consist of 501 tracks, repeat every 35 days, and are separated by about 0.75 degrees longitude. Ground tracks for TOPEX, ERS, and Geosat in the Yellow Sea are shown for 1 day, 0-5 days, 0-10 days, 0-15 days, 0-20 days, 0-25 days, 0-30 days, and 0-35 days in **Figure 5a-i**. TOPEX tracks are denoted by thick lines, Geosat tracks by medium thickness lines, and ERS by thin lines. On any one day in this region there may be as many as six ground tracks and as few as two ground tracks. For the Yellow and East China Seas region shown in **Figure 5**, there are 17 TOPEX ground tracks, 33 Geosat ground tracks, and 54 ERS ground tracks (**Figure 6**) possible without counting repeats. Over a period of 35 days and counting repeat tracks, there are 60 TOPEX tracks, 68 Geosat tracks, and 54 ERS tracks, which total 182 ground tracks.

Computation of climatological mean fields requires gridding of the data. Generally, squares are defined and average quantities are computed for each square. Averages can be computed by averaging all satellite data falling within a square for a specified time period, with equal weighting. However, a satellite crossing the middle of the square will contain many more instantaneous observations than a satellite crossing the square near an edge. The former (many-observation satellite) may provide a better estimate of the average state for that particular time, but only provides one independent estimate of the average state for that given time. The latter (fewer-observation satellite) also provides an independent estimate of the average state for another particular time within the specified time window. Hence, when combining multiple satellites, more representative average states are obtained by averaging the average values of individual satellite data within the grid square.

TOPEX, ERS, and Geosat hits of one-degree squares, not counting repeat hits, are shown in **Figure 7a** for averaging periods of up to 40 days. The number of grid square hits for each satellite increases at about the same rate, leveling off at 170 squares for TOPEX, 220 squares for Geosat, and 230 squares for ERS. The total number of non-terrestrial grids of the region is 235. ERS hits almost all one-degree squares in about 15 days and appears quite similar to the Geosat hits. TOPEX squares are repeated more than 3 times, and Geosat squares twice in 35 days, while ERS squares are not repeated. Similarly, hits for 0.5 and 0.25 degrees are shown in **Figures 7c** and **7e**. The percentage of hits in one-degree, half-degree, and quarter-degree squares are shown for the Yellow and East China Seas region in **Figures 7b**, **7d**, and **7f**. Maximum hit percentages for one-degree squares are 73 percent for TOPEX, 94 percent for Geosat, and 98 percent for ERS. For half-degree squares, hit percentages are much lower for Geosat and TOPEX (71 and 43 percent, respectively) while still about the same for ERS. For quarter-degree squares, maximum combined hit percentage for all three satellites is 85 percent with ERS accounting for more than half of the hits in individual squares. Within seven days 95 percent of the squares are hit at one-degree resolution and within 16 days 95 percent of the squares are hit at half-degree resolution. Only 75 percent of the squares at quarter-degree resolution are hit within seventeen days. For each grid resolution, all three satellite hits increase at about the same rate in time before leveling off and beginning their repeat patterns. The number of ground points used in the average state computations are approximately the same for each satellite (**Figure 8**) ranging near 10,000 points per satellite after 35 days.

Distributions of the number of hits in one-degree, half-degree, and quarter-degree squares for a combined TOPEX, ERS, and Geosat record are shown in **Figures 9a** and **9b** for 0 to 30 day periods and in **Figures 9c** and **9d** for 0 to 90 day periods. For 0 to 30 day periods, 10 hits per square occurs most commonly for one-degree squares, 5 hits per square occurs most commonly for half-degree squares, and 1 hit per square occurs most commonly for quarter-degree squares. For forming climatologies over 30 day periods, one-degree square distributions contain adequate observations to be representative. They are more gaussian in shape than the half-degree square distributions with at least 8 hits occurring about 60 percent of the time for the one-degree distribution and at least 4 hits occurring about 60 percent of the time for the half-degree resolution. Quarter degree resolution over 30 day periods is highly non-representative due to the low number of hits per square. One-half degree distributions are adequate for forming climatologies over 90 day periods since more than 10 hits per square occurs more than 60 percent of the time. Quarter-degree resolution would be marginal over 90 days since the hit distribution is non-gaussian and 60 percent of the squares contain less than 10 hits.

TOPEX, ERS, and Geosat hits by square are shown over a 30 day period for one-degree, half-degree, and quarter degree grids in **Figures 10a-10c**. Note that all of the one-degree squares and all but one of the half-degree squares are filled with hits. Numerous quarter degree squares are missed, but amount to only about 15 percent of the grid squares. More significant are the 1-counts in about 24 percent of the quarter-degree grid squares. Thus, almost 40 percent of the squares contain counts of 0 or 1 for the 30 day period. Hits by square are shown over a 90 day period in **Figures 11a-11c**. Averages in quarter degree squares are certainly more significant for the 90 day period since counts for the non-zero count squares are always at least 2. Minimum non-zero square count is 3 if three times the ERS period, 105 days, is used. Individual satellite counts over the 90 day period are shown for one-degree, half-degree, and quarter degree resolution in **Figures 12a-12c**. TOPEX, ERS, and Geosat are listed from top to bottom in each

square.

Assuming good data from all three satellites over 30 days, all one-degree squares will contain hits and all but one of the half-degree squares will contain hits. However, about 15 percent of the quarter-degree squares will not contain hits. A technique which has been used to grid TOPEX data on one-degree squares which contain no data entails expanding the search for data by half a square on each side. These one-degree data are then further interpolated to a quarter-degree grid for mapping purposes using an inverse distance averaging technique. An application of this processing procedure in the Yellow and East China Seas is presented in the next section. This technique can be applied to the half-degree and quarter-degree gridded data to fill out the grids.

3.2. Seasonal and annual climatology in the Yellow and East China Seas

In forming the climatological maps, the TOPEX data are averaged over one-degree squares. As discussed in the last section, not all one-degree squares contain TOPEX data. However, over 75% of the one-degree grid squares are supported by some data. Over a given time period, TOPEX data from one or more tracks that fall within any part of a square are used in the average for that square. Maximum allowable data values used in the averaging are 5 m for wave height and 20 m/s for wind speed. Major storms events are thereby excluded from the averaging. The data are then further interpolated to a 0.25 degree grid for smoothing purposes prior to contouring of the data by using an inverse-distance weighted averaging technique. Significant wave heights and wind speeds are processed for the 1993–1995 period. The analysis periods include the four seasons and annual mean for each year. Winter is defined as January through March, spring as April through June, summer as July through September, and fall as October through December. The region is controlled by the monsoon, producing predominantly northerly (Yellow Sea) and northeasterly (East China Sea) winds in the winter, and southeasterly to southwesterly winds for the whole region in the summer. Spring and autumn are transitional seasons for the region and wind velocities are more variable.

Figure 13 shows examples of the spatial distribution of significant wave height and wind speed for winter 1993 and summer 1994 (Hwang et al., 1998b, 1998c). As shown in these examples, the wind and wave fields exhibit significant structures and variations. In the winter season, the intensity distribution shows a well defined stratification with the gradient oriented in the northwest-southeast direction. The Kuroshio apparently exerts a strong influence on the wind speed and wave height, resulting in a local intensification of winds and waves.

Two distinctive regions of “hot spots” of winds and waves are found in the East China Sea. The first region consists of two hot spots, one in the Taiwan Strait and the other at the southeast of Taiwan. According to an account by Joe Wang (personal communication 1998), there are two famous Fong-Kous (Wind Mouths) near Taiwan: the first one is offshore of Hsinchu and the Penghu Channel (from Taichung Harbor to Penghu) in the Taiwan Strait. The second is the area offshore of SE Taiwan from Taitung to Erluanbee. Winds are stronger and waves are rougher in these locations than the surrounding areas during the winter monsoon. Lousanfong (the downhill draft or katabatic wind) is likely the main reason of the higher winds and rougher seas in these two areas. The central mountain range of Taiwan blocks the cold, NE winds from the sea. The air masses are forced to blow southward following the east coast of Taiwan. The air stream turns to the west at the southern tip of Taiwan, and induces strong winds in the SE region. The strong winds also generate higher waves. For the hot spot in Taiwan Strait, the air masses are forced to climb the mountain, producing significant rainfalls on the northeastern side of the mountain. A strong downhill draft is produced as these air masses pass the top of the mountain. Also, the horizontal geometry of the region is shaped like a funnel and contributes to the intensification of the northeasterly channeling through the Taiwan Strait.

The second region of intensified wind speeds and high waves is near Kyushu, Japan. The location of the hot spot is southwest of Kyushu in 1993, shifting southeastward to south of Kyushu in the two winter seasons of 1994 and 1995. The locations fall on the Kuroshio path near the Tokara Strait where it exits the East China Sea, and may indicate a region of strong air-sea interactions.

Another interesting location in this region is the Korea/Tsushima Strait, which is located at the

narrow portion of a geometry shaped like an hour glass. This geometry would favor a focusing or channeling of winds through the area. However, the region is in fact a local minimum of the wind and wave distributions. This is because the dominant wind direction in the Japan/East Sea is northwesterly during the winter, while the dominant wind in the East China Sea is northeasterly. Thus the Tsushima Strait is in fact in a divergent zone during the winter season and the winds and waves are relatively mild in the region.

During the summer season, the average wind speed is considerably lower. The high winds in various local hot spots range from 8 and 9 m/s, compared to 10.5 to 12.5 m/s for the winter season. The ridge structure of wind speed and wave height distributions oriented in the NE-SW direction still exists in the East China Sea, suggesting profound effects of the Kuroshio on the regional climatology. There is a hint of an oscillatory character in the spatial distribution of wind speeds, with a length scale of oscillation cycle on the order of 300 to 500 km. The average wave heights in the East China Sea shelf are considerably lower than those in the winter season, and the hot spots near Taiwan and Kyushu are no longer prominent. To the south of the Ryukyu Islands, high waves still prevail, with a 2.5 m seasonal average (essentially the same magnitude as the winter averages of regional hot spots) found near 126°E and 22°N.

3.3. Modification of winds and waves by the Kuroshio

The Yellow and East China Seas are on a large and shallow continental shelf, with depths less than 100 m in most of the region. The major current system in the region is the Kuroshio, which enters the East China Seas just southeast of Taiwan and exits just southwest of Japan. The main axis of the Kuroshio is usually just outside of the 200 m contour line (Figure 14). The Kuroshio may intrude onto the shelf in two regions. The first is through the Taiwan Strait during the winter months when the Taiwan Warm Current is weak (Chuang and Liang, 1983). The second source is the branching of the Tsushima Current from the Kuroshio (Lie and Cho, 1994) and the subsequent intrusion of the Yellow Sea Warm Current northward into the Yellow Sea (Hsueh, 1988). One of the driving forces of the Yellow Sea Warm Current and the flux of open ocean properties onto the continental shelf is the northerly wind bursts during the winter season. Due to the shallow water depth, the wind events are capable of creating large sea level changes, which produce horizontal pressure gradients that drive the subsurface currents (Hsueh, 1988).

The wind system is influenced by the monsoon wind pattern of Asia. In the winter, the Mongolian high-pressure system dominates the geostrophic winds and forms an anticyclonic gyre in the region. The primary wind direction in the winter months is northwesterly in the north, and northerly or northeasterly in the East China Sea. During the summer, the Indian Ocean low-pressure system dominates, creating a cyclonic gyre in the region. The wind direction is northwards to southeasterly in the whole region. During the transitional season between the two dominant weather systems, the winds fluctuate (Wang and Aubrey, 1983). The wave system is significantly affected by the wind system and other oceanographic processes such as the Kuroshio. Synoptic pictures of the seasonal climatology of winds and waves show surprisingly extensive details of the spatial structure (Figure 13). Most interesting of all, many of these features are found to be closely correlated to identifiable circulation systems including the Kuroshio and the Yellow Sea Cyclonic Eddy.

Based on our observations of the synoptic images and the different responses of winds and waves to the Kuroshio in different seasons, it is found that the wind speed and wave height are modified by the Kuroshio noticeably. Although the altimeter outputs only the wind speed and significant wave height, these two parameters are useful for investigating the modification of wave climate by the Kuroshio. This is because wave research over the years have provided a significant amount of knowledge on the correlation of wave heights and wind speeds under active wind generation as well as under the influence of swells on the wind-wave correlation (e.g., Hasselmann et al., 1973, 1976; Toba, 1978, 1997; Donelan, 1990). In fact, that knowledge has been put into use for deriving the characteristic wave periods of the wave field in the Gulf of Mexico from the altimeter measured wind speeds and significant wave heights, as described earlier. The resulting peak wave period and average wave period show excellent agreement with those measured from in situ ocean buoys (Hwang et al., 1998a). Briefly, it has been established from

decades of ocean wave measurements that in the case of active wind wave generation, the significant wave height and wind speed are related by a power law relationship,

$$H_s = AU_{10}^{\alpha}, \quad (12)$$

where H_s is the significant wave height, U_{10} is the neutral wind speed at 10 m reference height, A is a proportionality constant and α is the exponent of wind speed in the power law correlation. The exponent varies in a small range centered around 2. The variation may be attributed to the range of wind speeds, the fetch, duration, and other processes. Further discussion of this is out of the scope of this paper. The key point here is that this wind and wave power law correlation is significantly modified with the presence of swell, especially when the swell amplitude is large. The swell, though not locally generated, contributes to an increase of the observed significant wave height. Thus in a scatter plot of H_s versus U_{10} , the data points subject to swell influence will deviate from the active wind wave curve and bias high.

We have selected more than 20 stations on the TOPEX ground tracks, and examined the correlation of H_s and U_{10} for the winter and summer seasons. **Figure 15** displays the scatter plots of H_s versus U_{10} in six different locations: a and b are in the deep water region south of the Ryukyu Islands, c and d are in the Kuroshio, e is in the northern part of East China Sea, and f is in the middle of Yellow Sea. The coefficients in (12) are empirically determined to be $A=0.05$ and $\alpha=5/3$ for the Yellow and East China Seas region (shown as solid curves in **Figure 15**). As illustrated in the figure, the H_s - U_{10} correlation is significantly different in the summer and winter seasons. In particular, the winter data display the characteristics of active wind generation except for very low wind speed conditions (say, $U_{10}<6$ m/s). In the summer, the presence of swell component is quite obvious and many data points bias high compared to the empirical active generation curve established empirically. Most interesting of all, the swell "signature," which is found in almost the whole region, is significantly suppressed in the Kuroshio (compare cases with $U_{10}>6$ m/s in **Figure 15**).

As discussed in an earlier section, the wind condition in the Yellow and East China Seas region is dictated by the monsoon system and has distinct winter and summer seasons. The winter is characterized by northerly to northeasterly winds with relatively high wind speed. The summer wind is primarily southwesterly to southeasterly with relatively mild wind speed. Because the region is bounded by land on all three sides except on the south, the winter wave system is expected to exhibit the characteristics of active wind generation, while the summer wave system will have a strong contribution of swell components propagated from the opening in the southern side. The distinction of summer and winter wind/wave correlation is indeed confirmed from the TOPEX measurements. The results confirm our deduction of active wind wave characteristics for the winter season and swell influence in the summer season over the region except in the Kuroshio. The possible mechanisms of the suppression of swell signals by the Kuroshio may involve wave scattering in the interior and reflection at the boundaries. Although the detailed mechanisms remain to be identified and quantified, the observed suppression of swell signal can be used as a signature of the Kuroshio and other major circulation features. This will be further explored in the future.

3.4. Domains of winds and waves in the Yellow and East China Seas

As shown in Figure 13, there are considerable structure in the distribution of winds and waves in the Yellow and East China Seas. These structure in the spatial distribution can also be observed from ensemble averages of the wind speeds and wave heights along individual groundtracks. For example, Figure 16 shows the quarterly and annual averages of wind speeds and wave heights along groundtrack 69, which runs along the central axis of the Yellow and East China Seas region. The distinctive features described in the last two sections, such as the sheltering effect, the Kuroshio modification, and the summer swell, can be inferred. Based on those discussions, the wind and wave properties in the region defined by $(115^{\circ}\text{E}, 20^{\circ}\text{N})$ and $(130^{\circ}\text{E}, 42^{\circ}\text{N})$ can be divided into four major domains.

Yellow Sea: This domain (approximately north of 33.5°N) is surrounded by lands and peninsulas, with a small opening in the north connecting to Bohai and a big opening in the south connecting to the East

China Sea. The effects of coastal geometry and water depth are significant on the wave distribution, and to some degree also on the wind speed distribution. In the winter season, the wind speed and wave height along the Chinese coast are relatively low due to the shadowing effect of the Shandong Peninsula, as the dominant wind direction in the winter monsoon in this area is northerly. The structures of the wind and wave distributions generally follow an east-west stratification. In the summer time, winds and waves are predominantly southerly. The distributions become more zonal. Regions of low wind speeds and wave heights along the Chinese and Korean coasts are formed due to the shadowing effect of the neighboring coastal geometry.

Kuroshio: The effect of Kuroshio on the properties of wind and wave distributions is quite significant in all seasons except Summer. From observation of three years analysis (1993 to 1995), it is found that the immediate region of influence extends to 100 km on both sides of the Kuroshio axis. The wave heights and wind speeds along the Kuroshio axis are approximately 20% higher than those outside the region of immediate influence. The "signature" of the Kuroshio influence is most detectable in the half year from October to March. It is least obvious in the summer months, possibly due to a reduced air-sea temperature contrast. The Kuroshio appears to have a profound influence on the wind and wave distributions in the East China Sea also, to be discussed next.

East China Sea: With the Kuroshio bordering on the southern boundary, the wind and wave distributions are noticeably affected by the current. During the winter season, the orientation of the contours of wind speed and wave height distributions is northeast to southwest, following the general direction of the Kuroshio. Although the winter monsoon in this area is dominantly northeasterly, the wave height on the western side of this region, at a longer fetch, is in fact lower than that in the eastern side. In the summer time, the distribution of winds and waves in this domain is more cellular, with banded structure oriented along the northeast to southwest direction. The spatial distance of these oscillatory bands is roughly 300 to 500 km.

South of Ryukyu Islands: This domain is least affected by the land mass in the region. The wind and wave distributions in the region are characterized by cellular structure with spacing similar to those observed in the East China Sea. Although wind speeds in the summer season are significantly lower (by approximately 30 percent) than those in the winter months, the wave heights are comparable in both seasons in this domain.

4. Additional issues

4.1. Land proximity

While validation shows excellent agreement of wind speed and wave height between altimeter output and ocean buoy measurement in the open ocean, the comparison is generally poor in the coastal region, where large disagreements often occur. There are at least two major reasons for the large discrepancy in the nearshore measurements. First, the reflectivity of land and water are significantly different. Due to this difference, the signal level drops sharply in satellite approaches from land to sea, and rises drastically in sea to land approaches. As a result, the on-board auto gain control of the electronic circuit undergoes rapid changes. Since the wind and wave outputs represent average values of over 4000 pulses, these rapid changes in the electronic signals make the interpretation of the mean values (of wave form and signal intensity) difficult. The second reason is due to the greater spatial inhomogeneity of the coastal wave field within the radar footprint. Within the 7 km footprint size, the bottom bathymetry in the coastal region varies much more than in the deep water region. The terrestrial influence to the wind system also increases with the proximity of land. There are no established rules quantifying the deterioration of wind/wave data to the land proximity. Factors effecting the distance of data deterioration include the satellite approach (from land or from sea), the local bathymetry gradient, the plane geometry of the coastline, and other shoaling factors. From examining the satellite output, it is estimated that if the satellite approach is from land to sea, three to four footprint lengths (20 to 30 km) are needed for the signal to adjust to the change of backscattering characteristics between land and water. For the sea to land

approach, this distance is reduced to one footprint (7 km), but other factors mentioned above may dictate the application distance from land. Since the issue concerning land proximity has not been thoroughly investigated, as a conservative measure, data within at least 30 km of land should be excluded at this stage. To achieve a better coverage of the coastal region, reprocessing of the altimeter waveforms is necessary.

4.2. Combining multiple satellite measurements -- cross calibration

From the analysis presented in Section 3.1, it is clear that in order to have sub-degree or better-than-seasonal resolution, multiple satellite data are needed. Global comparisons with buoy data have shown significant differences among different satellite data suites. Cotton and Carter (1994) report the results on the cross calibration of TOPEX, ERS-1, and Geosat wave heights using available data up to 1994. The slopes of the linear best fit formulas for the four satellite wave products (Geosat, ERS-1 fast delivery (FD), ERS-1 ocean product (OPR), and TOPEX) vary from 0.663 to 1.010. The recent report of Cotton (1998) represents probably the most thorough analysis of satellite intercalibration. The formulas for obtaining "true" significant wave height and wind speed from Geosat, ERS-1, ERS-2, TOPEX and Poseidon data are listed below based on his study:

Geosat (1985-1989):

$$\begin{aligned} H_s &= 0.01185 + 1.1393H_{s(G)} \\ U_{10} &= 0.2775 + 0.8961U_{10(G)} \end{aligned} \quad (13)$$

ERS-1 (1991-1996):

$$\begin{aligned} H_s &= 0.3351 + 1.1091H_{s(E1)} \\ U_{10} &= 0.8453 + 0.8964U_{10(E1)} \end{aligned} \quad (14)$$

ERS-2 (1995-1997):

$$\begin{aligned} H_s &= 0.0350 + 1.0610H_{s(E2)} \\ U_{10} &= 0.8412 + 0.8767U_{10(E2)} \end{aligned} \quad (15)$$

TOPEX K_u band (1992-1997):

$$\begin{aligned} H_s &= -0.0942 + 1.0523H_{s(Tk)} \\ U_{10} &= 0.6796 + 0.8752U_{10(Tk)} \end{aligned} \quad (16)$$

POSEIDON (1992-1997):

$$\begin{aligned} H_s &= -0.0333 + 0.9791H_{s(P)} \\ U_{10} &= 0.6325 + 0.8609U_{10(P)} \end{aligned} \quad (17)$$

More recently, data drift in the significant wave height output of the TOPEX altimeter is noted. The details of the analysis are now under careful review and some results are available in unpublished manuscripts (Challenor and Cotton, 1998; Queffeulou, 1998; Nerem et al., 1998).

5. Summary and conclusions

This report presents a technical evaluation on the utility of wind and wave parameters derived from spaceborne altimeter measurements. Accuracies of the altimeter-measured wind speeds and wave heights have been validated with in situ oceanographic buoy measurements in several comparison studies. These results indicate that the measurements of wave height from spaceborne altimeters are essentially identical

to those obtained from ocean buoys. For co-located (10 km) and simultaneous (30 min) data sets, the correlation coefficient is better than 0.97, rms difference of 0.14 m, bias of 0.03 m, and proportionality coefficient of 0.99. The wind speed comparisons also are in very good agreement. For co-located and simultaneous data sets, the correlation coefficient and proportionality coefficient are 0.85 and 1.01; and the rms difference and the bias are 1.24 and 0.13 m/s, respectively.

One of the most important properties of spaceborne data set is the high-density spatial coverage. In the along track direction, the wind speeds and wave heights are reported every 7 km. Distances between neighboring tracks at the equator vary from less than 100 km for ERS to approximately 300 km for TOPEX. For higher latitudes these distances are much smaller. Global high-density coverage of wind and wave parameters cannot be achieved from any other means at the present stage.

Our analysis indicates that the climatology of wind speeds and wave heights can be constructed from TOPEX altimeter with a temporal resolution of 3 months and a spatial resolution of one degree. As an example, the seasonal and annual variations of winds and waves in the Yellow and East China Seas obtained from TOPEX are processed. The results reveal significant differences in the wind and wave distributions in the Yellow and East China Seas region. Based on these differences, the region is divided into four wind/wave domains: the Yellow Sea, the East China Sea, the Kuroshio, and south of Ryukyu Islands. The domains or provinces of these distinct regions can be associated to local geometry and bathymetry (e.g., Yellow Sea domain) or special oceanographic processes (e.g., Kuroshio domain). The climatology obtained from the spaceborne altimeter is in excellent agreement with that expected from the monsoon seasons in this region of the world. Using Geosat Follow-On or ERS, the spatial resolution can be improved, but temporal resolution deteriorates. By combining multiple satellites, monthly climatologies for 0.5° or even 0.25° resolution can be achieved.

It is concluded that spaceborne altimeters provide excellent measurements of wind speeds and wave heights at a high spatial density. The accuracy of these environmental parameters is statistically comparable to that of ocean buoy measurements. These measurements represent an excellent data source for regional and global wind/wave climatology studies.

Acknowledgment

This research is sponsored by the U.S. Naval Oceanographic Office and the U.S. Army Corps of Engineers, Coastal and Hydraulic Laboratory. Gregg Jacobs was instrumental in extracting the satellite altimetry data. We also acknowledge the constructive discussions with Steve Bratos and Don Resio. [NRL contribution MR/7332—98-8216].

Appendix I. Comparison of altimeter and buoy measurements of wind speed and wave height

A. Significant wave height

Comparisons of TOPEX significant wave heights (H_s) with in-situ measurements from surface buoys have shown very positive agreement (e.g., Carter et al., 1992; Cotton and Carter, 1994; Ebuchi and Kawamura, 1994; Gower, 1996). In particular, Gower (1996) presents a comprehensive comparison of wind speed and wave height between TOPEX altimeter measurements and 14 moored buoys along the West Coast of Canada, of which 3 are in the open ocean, approximately 400 km west of the British Columbia coast; 6 are in the exposed positions within 100 km from the coast, and 5 are in sheltered coastal waters. He performed detailed statistical comparisons of these three groups of buoys with all three altimeters (NASA Ku- and C-band altimeters and CNES Ku-band solid state altimeter) on TOPEX/POSEIDON. The temporal difference between TOPEX and buoy measurements is less than 30 minutes, and the spatial distance less than 107 km. An excellent agreement between the altimeter and buoy measurements of the significant wave height is found for the nine buoys in exposed positions. From the Ku-band data, the fitted slope of the scatter plots is 0.94 for the three outer buoys and 0.98 for the six inner buoys. The rms differences are 0.35 and 0.30 m, respectively for these two data groups. For coastal

regions, the agreement deteriorates, with fitted slopes ranging from 0.85 to 1.33, and rms differences ranging from 0.24 to 0.60 m. The large variation in the coastal comparison is attributed to the local variation of the wave conditions due to the close proximity to the shoreline. Gower (1996) further shows that in the exposed locations, the rms data scatter is greatly reduced when the spatial distance between TOPEX and buoy observations is reduced to 10 km. For the three outer buoys, it reduces from 0.35 to 0.14 m, and for the 6 inner buoys, from 0.30 to 0.15 m. The fitted slopes also improved, from 0.94 to 0.97, and 0.98 to 1.00 for the outer and inner groups, respectively. From these results, we may conclude that the output of significant wave height from the TOPEX altimeter, at 1336 km above ocean, is essentially identical to the surface buoy observation.

The excellent agreement on the wave height measurement is also confirmed in the Gulf of Mexico stations. The comparison with five buoys in the Gulf of Mexico is presented in Hwang et al. (1998a). The comparison period covers the period from October 1992 to December 1995, or 3.15 years. Because surface buoys collect wave data every hour, buoy data points before and after the TOPEX time are selected for comparison with each TOPEX data point. The wind and wave data from NDBC buoys are acquired and reported hourly. The significant wave height and peak wave period are derived from the buoy heave motion spectrum measured over a 20-minute acquisition period starting at 30 minutes after the hour. The wind speed and wind direction are collected by a wind sensor located on the buoy's mast. The elevation of the wind sensor is 5 m above the sea level. The wind speed and wind direction are the vector-averages over the 8-minute acquisition period starting at 42 minute after the hour. For the comparison to the TOPEX data acquisition time, the representative data acquisition time for the hourly buoy wind and wave data is assigned at 40 minutes after the previous hour (that is, the acquisition time is 10:40 for the buoy report time 11:00). The comparison time is therefore at the middle of the wave data acquisition period, and 6 minutes before the mid-point of the wind record. The buoy data points are separated into two groups. The time lags (TOPEX acquisition time minus buoy acquisition time) of the first group are less than 0.5 hour, with an average (T_1) near 0.25 hour. The time lags for the second group are greater than 0.5 but less than 1 hour, with an average (T_2) of approximately 0.75 hour. Agreements between the altimeter and buoy measurements for most of the data sets compiled are excellent, except for the coastal station (Buoy 42035). **Figure 2a** shows an example of the scatter plot of wave heights measured by TOPEX and NDBC. To reflect the density of data on each plotted point in the **figure**, the size of the plotting symbol is adjusted to be proportional to the number of data points falling in the same plotting coordinates. More objectively, key statistical parameters are calculated and listed in Hwang et al. (1998a).

B. Wind speed

The derivation of wind speed from microwave radars is based on the correlation of surface roughness and radar backscattering intensity (the normalized radar backscattering cross section, σ_0). For the spaceborne altimeters, specular reflection is the primary mechanism of radar backscatter. In this mode, roughness on the surface causes incident waves to diffuse and scatter away from the aperture of radar reception, and the rougher the surface the less backscattering cross section is expected. On the ocean surface, short ocean waves are the primary contributor to the surface roughness (Cox and Munk, 1954; Hwang and Sheinin, 1988; Hwang et al., 1996; Hwang, 1997). Because these short water waves are wind generated, a higher σ_0 corresponds to a lower wind speed and vice versa. Over the past two decades, however, the operational algorithms to retrieve wind speed from the altimeter backscattering cross section have been based on empirical formulae. These formulae are either established on collocated databases of altimeter and surface in-situ measurements (e.g., Brown et al., 1981; Chelton and Wentz, 1986; Witter and Chelton, 1991) or based on the statistical distributions of wind speed and σ_0 separately (Freilich and Challenor, 1994). Many comparisons of various algorithms (e.g., Witter and Chelton, 1991; Wu, 1992; Freilich and Challenor, 1994) have shown that despite of the continuous improvement of the altimeter hardware and software, the progress of wind speed retrieval from various algorithms developed over the last 20 years remains stagnant. For example, Freilich and Challenor (1994) report a very comprehensive

analysis of eight algorithms. Results in terms of the mean error, root mean square error, standard deviation, wind speed error trend and pseudo-wave age error trend are tabulated. The differences in all eight algorithms are relatively minor. In terms of the mean square error and standard deviations, 7 of the 8 algorithms produced less than 10% differences in these two key parameters (1.60 to 1.75 m/s rms difference, 1.58 to 1.72 m/s standard deviation). **Figure 2b** shows the distributions of the wind speed derived by the MCW algorithm (modified Chelton and Wentz, Witter and Chelton, 1991) compared to the buoy measurements.

C. Wave period

It is generally recognized that in a wind-generated ocean wave system, there is a close correlation among the three key parameters of the wave field: wind speed, wave height and wave period. Such correlation has been established through theoretical analysis of wave dynamics and confirmed with ocean wave measurements (e.g., Hasselmann et al., 1973, 1976; Toba, 1978, 1997). Hasselmann et al. (1973, 1976) discuss the fetch dependence of one-dimensional spectra and establish the three key dimensionless wave parameters, the peak frequency, $f_m^* = f_m U_{10}/g$; the fetch, $x^* = xg/U_{10}^2$; and the total wave energy, $E^* = g^2 E/U_{10}^4$; where $*$ denotes the dimensionless parameters and g is the gravitational acceleration. They show that the three parameters are closely related by the following equations:

$$f_m^* = 35x^*^{-0.33}, \quad (I-1)$$

and

$$E^* = 1.6 \times 10^{-7} x^*. \quad (I-2)$$

The linear equation (I-2) can be substituted into (I-1) to derive the functional relationship of the wave frequency, wind speed and wave energy and eliminate the fetch parameter. The formula relating the three parameters, wind speed (U_{10}) wave height (H_s) and the characteristic wave period (T) can be derived using the relations $E = \eta_{RMS}^2$, $H_s = 4\eta_{RMS}$, and the inverse relation of wave period and wave frequency. The quantity η_{RMS} is the root mean square of the sea surface displacement. In the original derivation the peak wave period, T_p , of the wave spectrum was used as the characteristic wave period based on several groups of experimental data. The resulting equation is

$$\frac{U_{10}}{gT_p} = 4.8 \times 10^{-2} \left(\frac{U_{10}^2}{gH_s} \right)^{2/3}. \quad (I-3)$$

The tight correlation between U_{10}/gT_p and U_{10}^2/gH_s is also found in the Gulf of Mexico wave data (Hwang et al., 1998a). The bias and the symmetric regression coefficient (Bauer et al., 1992) for the fitting are, respectively, 0.006 and 1.05 for the time-lag group-1 data and 0.002 and 1.00 for the time-lag group-2 data. The correlation function was established based on a “saturated” sea condition that characterizes the local-wind generated wave system. When swells from distant wind sources are present, the correlation needs to be modified. The Gulf of Mexico, being a semi-enclosed sea, is found to be less dominated by long swell systems. From experience of analyzing the Gulf of Mexico wave data, it is found that the wave energy associated with the swell frequency rarely exceeds 15 percent of the total spectral energy in the region. Although we have not tested this procedure to calculate the wave frequency from altimeter data in other regions of the world, it is noticed that (I-3) is a very robust equation relating the wave period to the wind speed and wave height. The effect of swells will modify mainly the significant wave height derived by the sensor. Because the wave period is related to the wave height as $T \sim H_s^{2/3}$ (I-3), the error introduced by swell presence can be quantified. For example, if the spectral intensity in the swell-sea system doubles by the presence of swells, the wave height of the saturated sea will be overestimated by a factor of $2^{1/2}$ (square root of 2), and introduce an overestimation of wave period by approximately 25 percent.

Based on the experience from analyzing the wave spectrum it is found that the peak wave period is an unstable quantity and may show a large variation when different data processing procedures are used. Alternatively, the average wave period, T_a (calculated from the wave spectrum by $T_a = [\int f^2 S(f) df / \int S(f) df]^{1/2}$, where f is the wave frequency and $S(f)$ is the frequency spectrum) can be used in place of the peak wave period. Because T_a is an integrated property, it is more robust than T_p . Both T_p and T_a are standard output of the NDBC buoy data set. The plot of U_{10}/gT_a vs. U_{10}^2/gH_s of the Gulf of Mexico data indicates a comparable tight grouping of the two dimensionless parameters as those of U_{10}/gT_p vs. U_{10}^2/gH_s (Hwang et al., 1998a). The trend is slightly different from (I-3). Empirically, the following equation provides good agreement with the buoy measurements in the Gulf of Mexico,

$$\frac{U_{10}}{gT_a} = 6.0 \times 10^{-2} \left(\frac{U_{10}^2}{gH_s} \right)^{0.6} \quad (I-4)$$

The bias and the symmetric regression coefficient are, respectively, -0.008 and 0.94 for the group-1 data, and -0.012 and 0.91 for the group-2 data.

The ratio of T_p/T_a tends to be rather constant. The average ratio with one standard deviation is 1.29 ± 0.14 . In either case of using T_p or T_a as the characteristic wave period, the data points collapse together and follow the functional forms suggested by (I-3) and (I-4) very well (Hwang et al. 1998a). It is therefore expected that using the TOPEX altimeter output, the characteristic wave period of the wave field can be derived using either (I-3) for the peak period or (I-4) for the average period.

From the above discussion, it is conceivable that the altimeter data can also provide the characteristic period of a wave field. It has been established that the precision of wind speed and wave height measurements from the altimeter is quite high, and thus we expect that the wave period derived from the TOPEX output will be also comparable to the measurement from in-situ buoys. **Figure 2c** shows an example of the characteristic (average) wave period, T_a , calculated from (I-4) using the altimeter-derived wind speed (MCW algorithm) and wave height, plotted against the buoy-measured average period.

References

Bauer, E., S. Hasselmann, and K. Hasselmann, Validation and assimilation of Seasat altimeter wave heights using the WAM wave model, *J. Geophys. Res.*, 97, 12671-12682, 1992.

Brown, G. S., H. R. Stanley, and N. A. Roy, The wind speed measurement capability of spaceborne radar altimeters, *IEEE J. Oceanic Eng.*, OE-6, 59-63, 1981.

Carter, D. J. T., P. G. Challenor, and M. A. Srokosz, An assessment of Geosat wave height and wind speed measurements, *J. Geophys. Res.*, 97, 11383-11392, 1992.

Challenor, P., and P. D. Cotton, Trends in TOPEX significant wave height measurement, Southampton Oceanography Center, Southampton, SO14 3ZH, UK, 5 pp, 1998.

Chelton, D. B., and F. J. Wentz, Further development of an improved altimeter wind speed algorithm, *J. Geophys. Res.*, 91, 14250-14260, 1986.

Chelton, D. B., E. J. Walsh, and J. L. MacArthur, Pulse compression and sea level tracking in satellite altimetry, *J. Atm. and Oceanic Tech.*, 6, 407-438, 1989.

Chuang, W. S., and W. D. Liang, Seasonal variability of intrusion of the Kuroshio water across the continental shelf northeast of Taiwan, *J. Oceanogr.*, 50, 531-542, 1994.

Cotton, P. D., A feasibility study for a global satellite buoy intercalibration experiment, Tech. Rep., Southampton Oceanography Center, 73pp, 1998.

Cotton, P. D., and D. J. T. Carter, Cross calibration of TOPEX, ERS-1, and Geosat wave heights, *J. Geophys. Res.*, 99, 25025-25033, 1994.

Cox, C. S., and W. Munk, Statistics of the sea surface derived from sun glitter, *J. Mar. Res.*, 13, 198-227, 1954.

Donelan, M., Air-sea interaction, in *The Sea: Ocean Engineering Science*, 9, 239-292, 1990.

Ebuchi, N., and H. Kawamura, Validation of wind speeds and significant wave heights observed by the TOPEX altimeter around Japan, *J. Oceanography*, 50, 479-487, 1994.

Freilich, M. H., and P. G. Challenor, A new approach for determining fully empirical altimeter wind speed model functions, *J. Geophys. Res.*, 99, 25051-25062, 1994.

Fu, L.-L, E. J. Christensen, and C. A. Yamarone, TOPEX /POSEIDON mission overview, *J. Geophys. Res.*, 99, 24369-24381, 1994.

Gower, J. F. R., Intercomparison of wave and wind data from TOPEX/POSEIDON, *J. Geophys. Res.*, 101, 3817-3829, 1996.

Hasselmann, K., T. P. Barnett, E. Bouws, H. Carlson, D. E. Cartwright, K. Enke, J. A. Ewing, H. Gienapp, D. E. Hasselmann, P. Kruseman, A. Meerburg, P. Muller, D. J. Olbers, K. Richter, W. Sell, and H. Walden, Measurements of wind-wave growth and swell decay during the Joint North Sea Wave Project (JONSWAP), Erganzungsheft zur Deutschen Hydrographischen Zeitschrift, Reihe A(8), Nr. 12, Deutschen Hydrographischen Institut, Hamburg, Germany, 95 pp, 1973.

Hasselmann, K., D. B. Ross, P. Miller, and W. Sell, A parametric wave prediction model, *J. Phys. Oceanogr.*, 6, 200-228, 1976.

Hsueh, Y., Recent current observations in the Eastern Yellow Sea. *J. Geophys. Res.*, 93, 6875-6884, 1988.

Hsueh, Y., C.-S. Chern, and J. Wang, Blocking of the Kuroshio by the continental shelf northeast of Taiwan, *J. Geophys. Res.*, 98, 12351-12359, 1993.

Hwang, P. A., A study of the wavenumber spectra of short water waves in the ocean. Part 2. Spectral model and mean square slope, *J. Atm. and Oceanic Tech.*, 14, 1174-1186, 1997.

Hwang, P. A., and O. H. Shemdin, The dependence of sea surface slope on atmospheric stability and swell condition, *J. Geophys. Res.*, 93, 13903-13912, 1988.

Hwang, P. A., S. Atakturk, M. A. Sletten, and D. B. Trizna, A study of the wavenumber spectra of short water waves in the ocean, *J. Phys. Oceanogr.*, 26, 1266-1285, 1996.

Hwang, P. A., W. J. Teague, G. A. Jacobs, and D. W. Wang, A statistical comparison of wind speed, wave height and wave period derived from satellite altimeters and ocean buoys in the Gulf of Mexico region, *J. Geophys. Res.* 103, 10451-10468, 1998a.

Hwang, P. A., W. J. Teague, G. A. Jacobs, and D. W. Wang, Wind and waves in the Yellow and East China Seas from satellite altimeter measurement, *Pacific Ocean Remote Sensing Conference*, 1, 321-325, 1998b.

Hwang, P. A., S. M. Bratos, W. J. Teague, D. W. Wang, G. A. Jacobs, and D. T. Resio, Winds and waves in the Yellow and East China Seas: Spaceborne altimeter measurements and model results, subm. to *J. Oceanogr.*, 1998c.

Lie, H. J., and C. H. Cho, On the origin of the Tsushima Warm Current, *J. Geophys. Res.*, 99, 25081-25091, 1994.

Nerem, R. S., D. P. Chambers and T. J. Urban, Unusual TOPEX/POSEIDON measurements during 1997-1998 ENSO event. Memo to Joint TOPEX/POSEIDON-Jason-1 Science Team, Center for Space Research, The University of Texas at Austin, 3925 West Braker Lane, Suite 200, Austin, Texas 78759-5321, USA, 8pp, 1998.

Queffeuilou, P., Long-term comparison of ERS, TOPEX, and POSEIDON altimeter wind and wave measurements, Institut Français de Recherché pour l'Exploitation de la Mer, Département d'Oceanographie Spatiale, BP70, 29280 Plouzané, France, 6 pp, 1998.

Toba, Y., Stochastic form of the growth of wind waves in a single-parameter representation with physical interpretation, *J. Phys. Oceanogr.*, 8, 494-507, 1978.

Toba, Y., Wind forced strong interactions and quasi-local equilibrium between wind and windsea with the friction velocity proportionality, in *Nonlinear Ocean Waves*, ed. W. Perrie, Computational Mechanics Publ., Southampton, Great Britain, 1-59, 1997.

Wang, Y., and D. G. Aubrey, The characteristics of China Coastline. *Cont. Shelf Res.*, 7, 329-349, 1987.

Witter, D. L., and D. B. Chelton, A Geosat altimeter wind speed algorithm and a method for altimeter wind speed algorithm development, *J. Geophys. Res.*, 96, 8853-8860, 1991.

Wu, J., Near-nadir microwave specular returns from the sea surface - altimeter algorithm for wind and wind stress, *J. Atm. Oceanic Tech.*, 9, 659-667, 1992.

List of tables

Table 1. Statistics of TOPEX - Buoy Comparisons

A. Significant Wave Height, H_s

Source	Bias	RMS	Intercept	Slope	Regress. Coef.	Correlation Coefficient
	(m)	(m)	(m)			
Ebuchi and Kawamura(1994)						
Average of 5 closest points within 150 km	0.32	0.45	-----	-----	-----	-----
Gower (1996) <10 km						
Outer (deep)	-----	0.14	-0.11	1.00	0.97	-----
Inner (exposed)	---	0.15	0.05	0.99	1.00	-----
Coastal (protected)	-----	0.14	0.08	0.98	1.01	-----
Hwang et al. (1998)						
<20km	-0.05	0.17	0.14	0.86	0.95	0.98
<10 km	-0.02	0.14	0.12	0.89	0.99	0.97

B. Wind Speed, U_{10}

	(m/s)	(m/s)	(m/s)			
Ebuchi and Kawamura(1994)	0.18	1.77	-----	-----	-----	-----
Gower (1996) <10 km						
Outer (deep)	-----	1.35	-1.39	1.28	1.12	-----
Inner (exposed)	-----	1.76	-0.54	1.11	1.04	-----
Hwang et al. (1998)						
<20km	-0.23	1.24	0.40	0.90	0.98	0.88
<10 km	0.13	1.24	1.23	0.83	1.01	0.85

C. Wave Period, T_a

	(s)	(s)	(s)			
Hwang et al. (1998)						
<20km	0.56	1.00	-2.10	1.54	1.14	0.85
<10km	0.35	0.63	-1.10	1.30	1.08	0.87

List of figures

Figure 1. A sketch illustrating the modification of radar wave forms by surface waves of different significant heights.

Figure 2. Comparison of the altimeter and buoy measurements of the significant wave height (a), wind speed (b), and characteristic (average) wave period (c). Only data points with spatial lags less than 10 km are included in this comparison. The size of the plotting symbol is proportional to the data density. The ratios (TOPEX measurements divided by buoy measurements) of these three wave parameters are shown in (d), (e) and (f), respectively.

Figure 3. An example of discriminating sea and swell conditions using Eq. (7). (a) Plot of H_s vs. U_{10} . o: buoy measurements, x: TOPEX data, the region above the solid curve represents swell contribution. (b) The ratio of swell to sea as a function of wind speed for database T115B220. (c) The time of swell cases measured by buoy (o) and TOPEX (x). This plot shows that most of the swell cases identified from the two data sources (buoy and TOPEX) are the same ones.

Figure 4. Along track distribution of wind speed (solid curve) and wave height (dashed curve), multiplied by 5. Eight satellite passes are shown.

Figure 5. ERS (thin lines), Geosat (medium thickness lines), and TOPEX (thick lines) ground tracks in the Yellow and East China Seas region. (a) day 1, 1996, (b) day 2, (c) days 0-5, (d) days 0-10, (e) days 0-15, (f) days 0-20, (g) days 0-25, (h) days 0-30, (i) days 0-35. Note that the total number of ground tracks vary slightly for other periods.

Figure 6. Number of ground tracks in the Yellow and East China Seas region, counting repeated tracks, as a function of time. TOPEX, ERS, and Geosat tracks are denoted by solid, dashed, and dashed-and-dotted lines, respectively.

Figure 7. (a) Number of one-degree squares hit by TOPEX, ERS, and Geosat over 40 days. TOPEX, ERS, and Geosat tracks are denoted by solid, dashed, and dashed-and-dotted lines, respectively. (b) Percentage of one-degree squares hit in the Yellow and East China Seas region by TOPEX (solid), ERS (dashed), Geosat (dashed-and-dotted), and combined (dotted) tracks over a 40 day period. (c, d) Same as in (a, b) but for half degree squares. (e, f) Same as in (a, b) but for quarter degree squares.

Figure 8. Number of ground points in the Yellow and East China Seas region for TOPEX (solid), ERS (dashed), and Geosat (dashed-and-dotted) over a 35-day period.

Figure 9. (a) Histograms, and (b) cumulative distributions of number of ground track hits for combined TOPEX, ERS, and Geosat tracks over a 30-day period for one-degree (solid), half degree (dashed), and quarter degree (dashed-and-dotted) squares. (c, d) same as (a, b) but for a 90-day period.

Figure 10. Distribution of combined TOPEX, Geosat, and ERS ground track hits for days 0-30, (a) one-degree squares, (b) half degree squares, and (c) quarter degree squares.

Figure 11. Distribution of combined TOPEX, Geosat, and ERS ground track hits for days 0-90, (a) one-degree squares, (b) half degree squares, and (c) quarter degree squares.

Figure 12. Distribution of individual TOPEX, Geosat, and ERS ground track hits for days 0-90, (a) one-degree squares, (b) half degree squares, and (c) quarter degree squares. Counts in each square reflect TOPEX, ERS, and Geosat from top, middle, and bottom, respectively.

Figure 13. The seasonal climatology of winds and waves in the Yellow and East China Seas. Winter 1993: (a) H_s , (b) U_{10} ; Summer 1994: (c) H_s , (d) U_{10} .

Figure 14. TOPEX ground tracks in the Yellow and East China Seas region and the local bathymetry. The seasonal averages of the Kuroshio axes are superimposed. Squares indicate the locations where the correlation of wind speeds and wave heights are investigated and partially plotted in Figure 15.

Figure 15. The scatter plots of H_s versus U_{10} several regions of the Yellow and East China Seas. (a) and (b) in deep water south of the Ryukyu Islands; (c) and (d) in the Kuroshio; and (e) and (f), in the middle of East China Sea and Yellow Sea.

Figure 16. ensemble averages of (a) wind speed, and (b) wave height distributions along groundtrack 69 in the Yellow and East China Seas region. The results are based on averaging four years (1993-1997) of TOPEX output. o: quarter 1, x: quarter 2, +: quarter 3, \square : quarter 4, \diamond : annual average.

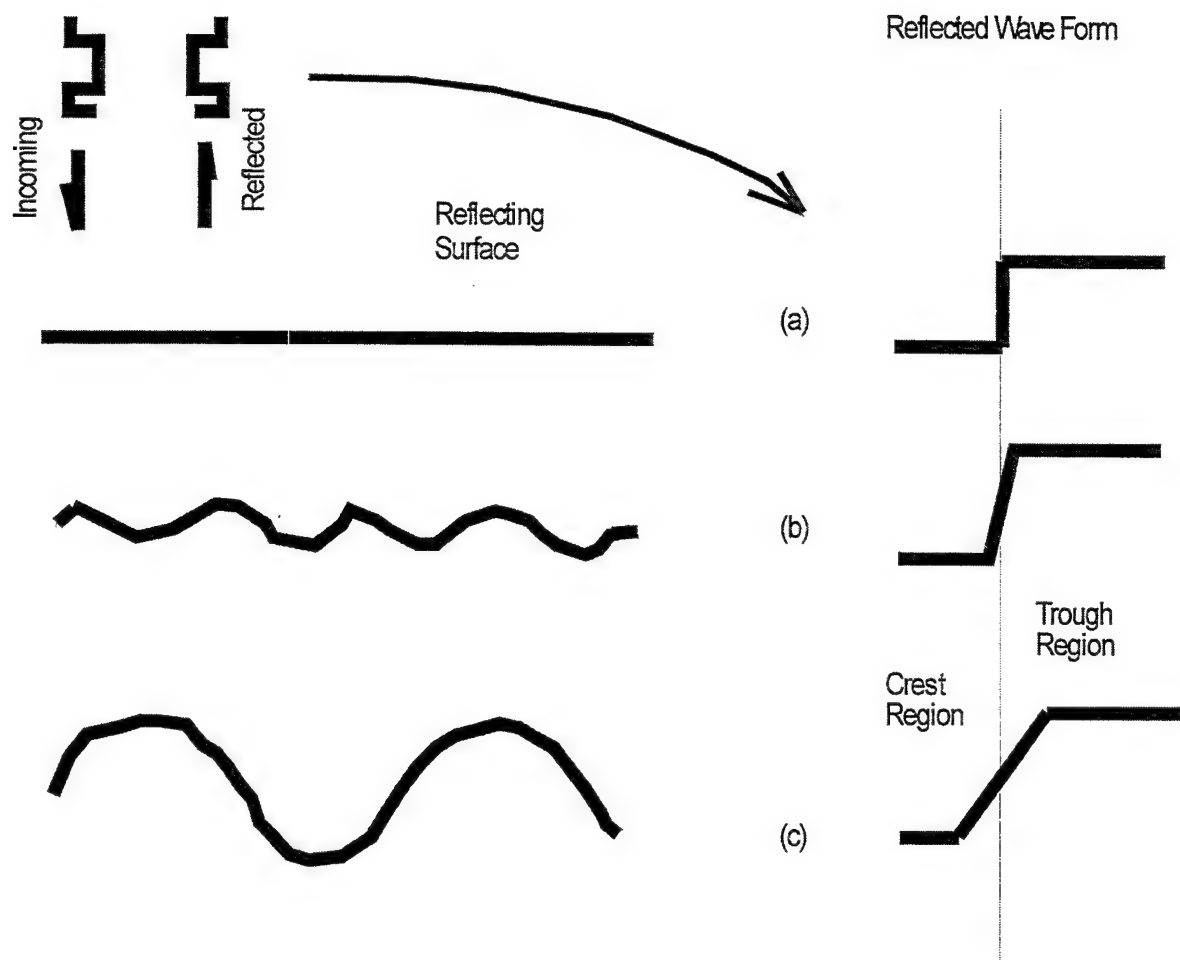


Figure 1. A sketch illustrating the modification of radar wave forms by surface waves of different significant heights.

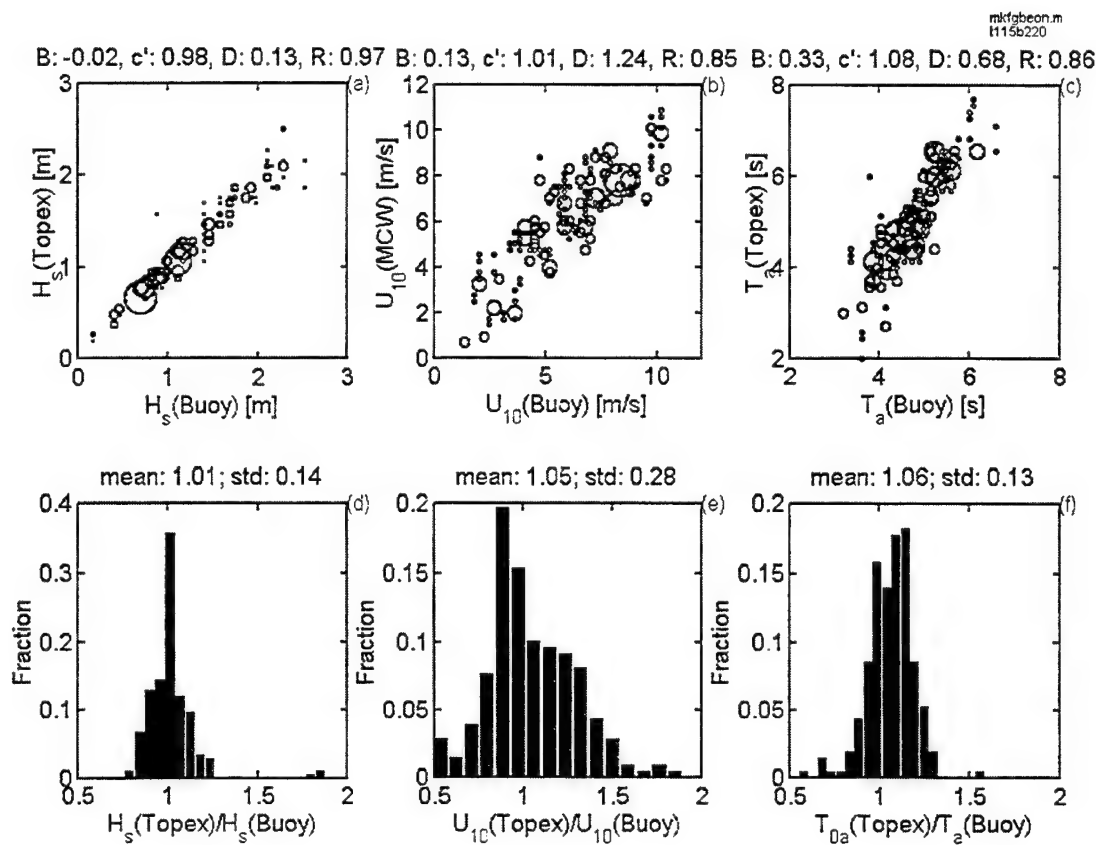


Figure 2. Comparison of the altimeter and buoy measurements of the significant wave height (a), wind speed (b), and characteristic (average) wave period (c). Only data points with spatial lags less than 10 km are included in this comparison. The size of the plotting symbol is proportional to the data density. The ratios (TOPEX measurements divided by buoy measurements) of these three wave parameters are shown in (d), (e) and (f), respectively.

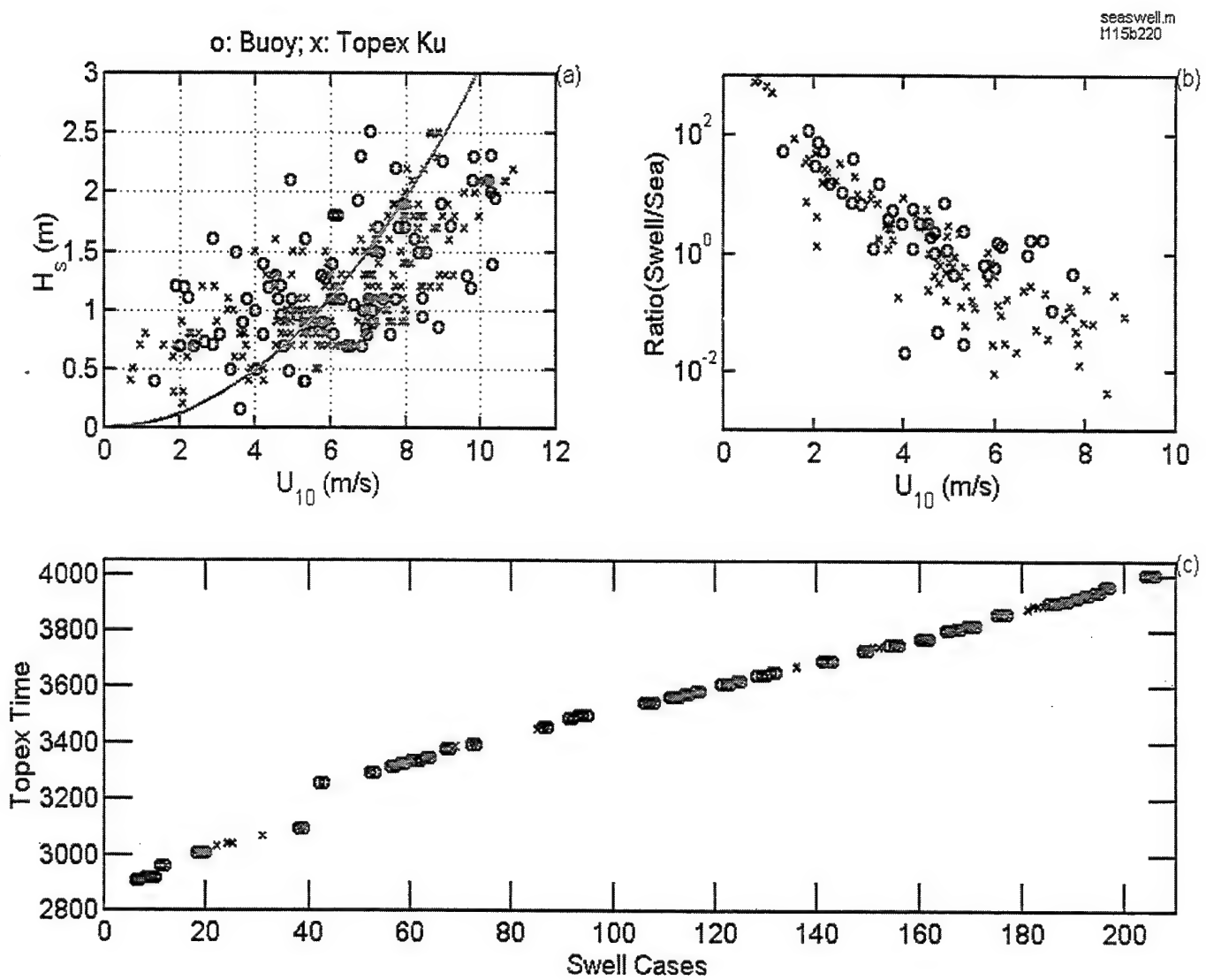


Figure 3. An example of discriminating sea and swell conditions using Eq. (7). (a) Plot of H_s vs. U_{10} . o: buoy measurements, x: TOPEX data, the region above the solid curve represents swell contribution. (b) The ratio of swell to sea as a function of wind speed for database T115B220. (c) The time of swell cases measured by buoy (o) and TOPEX (x). This plot shows that most of the swell cases identified from the two data sources (buoy and TOPEX) are the same ones.

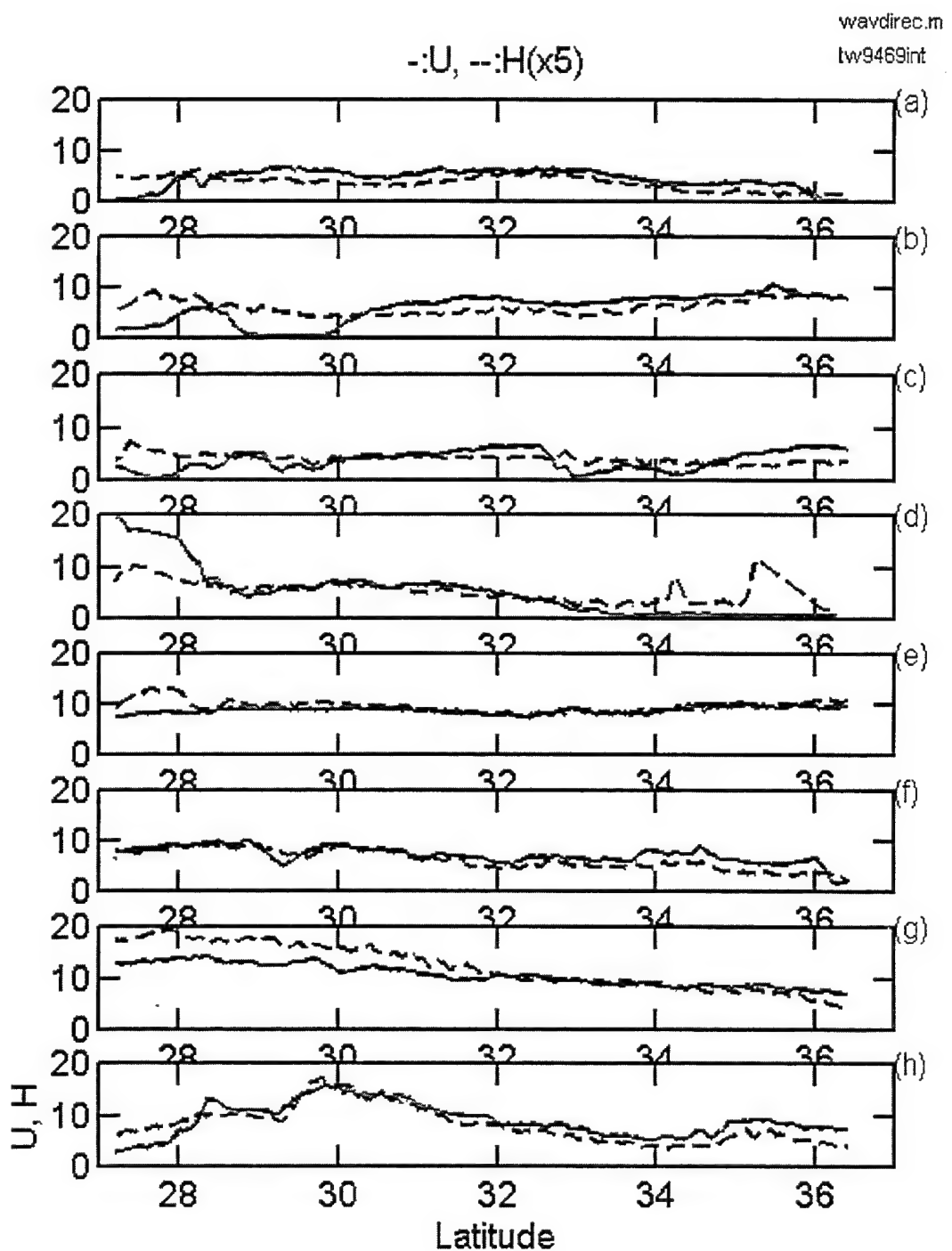


Figure 4. Along track distribution of wind speed (solid curve) and wave height (dashed curve), multiplied by 5. Eight satellite passes are shown.

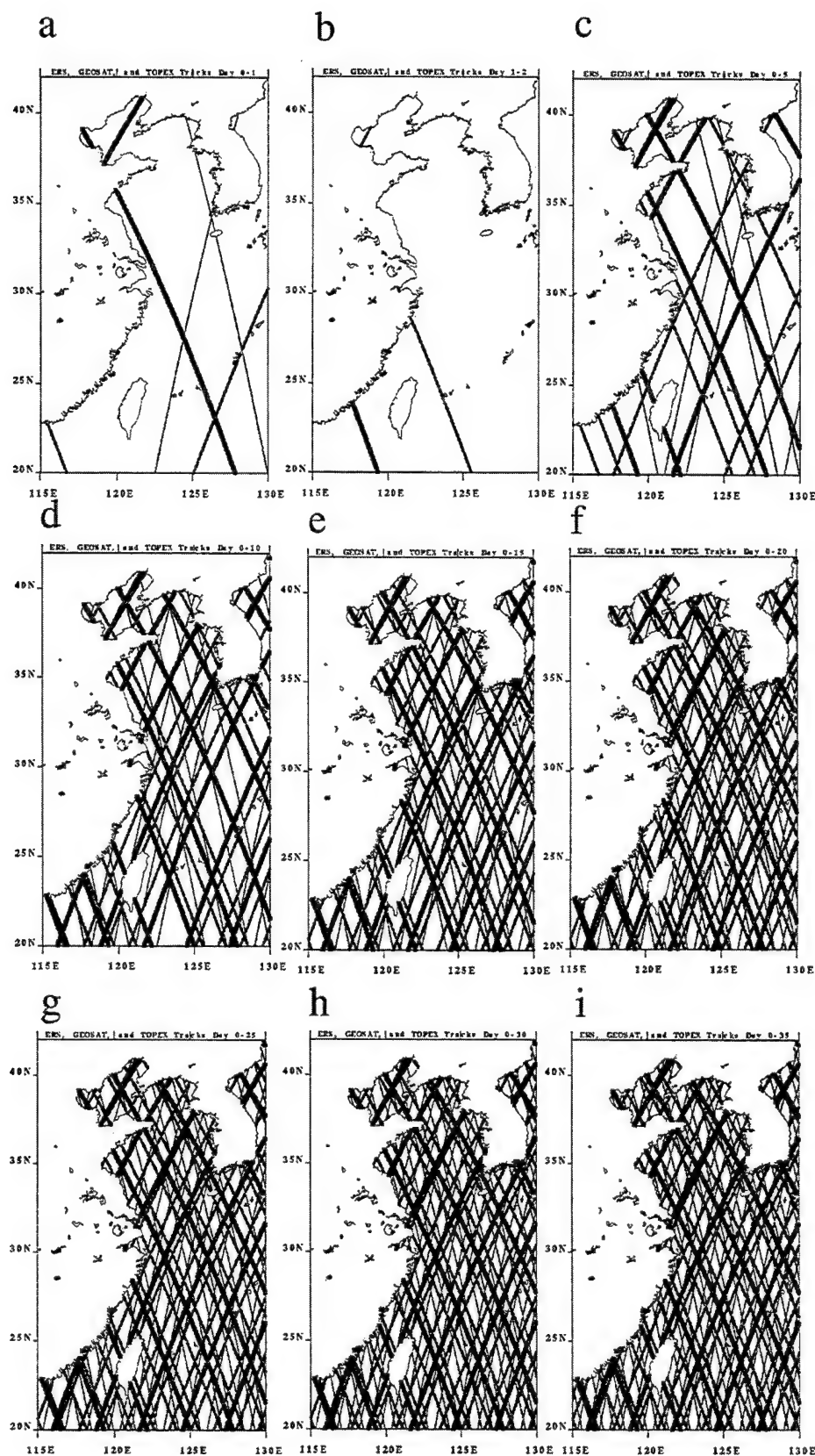


Figure 5. ERS (thin lines), Geosat (medium thickness lines), and TOPEX (thick lines) ground tracks in the Yellow and East China Seas region. (a) day 1, 1996, (b) day 2, (c) days 0-5, (d) days 0-10, (e) days 0-15, (f) days 0-20, (g) days 0-25, (h) days 0-30, (i) days 0-35. Note that the total number of ground tracks vary slightly for other periods.

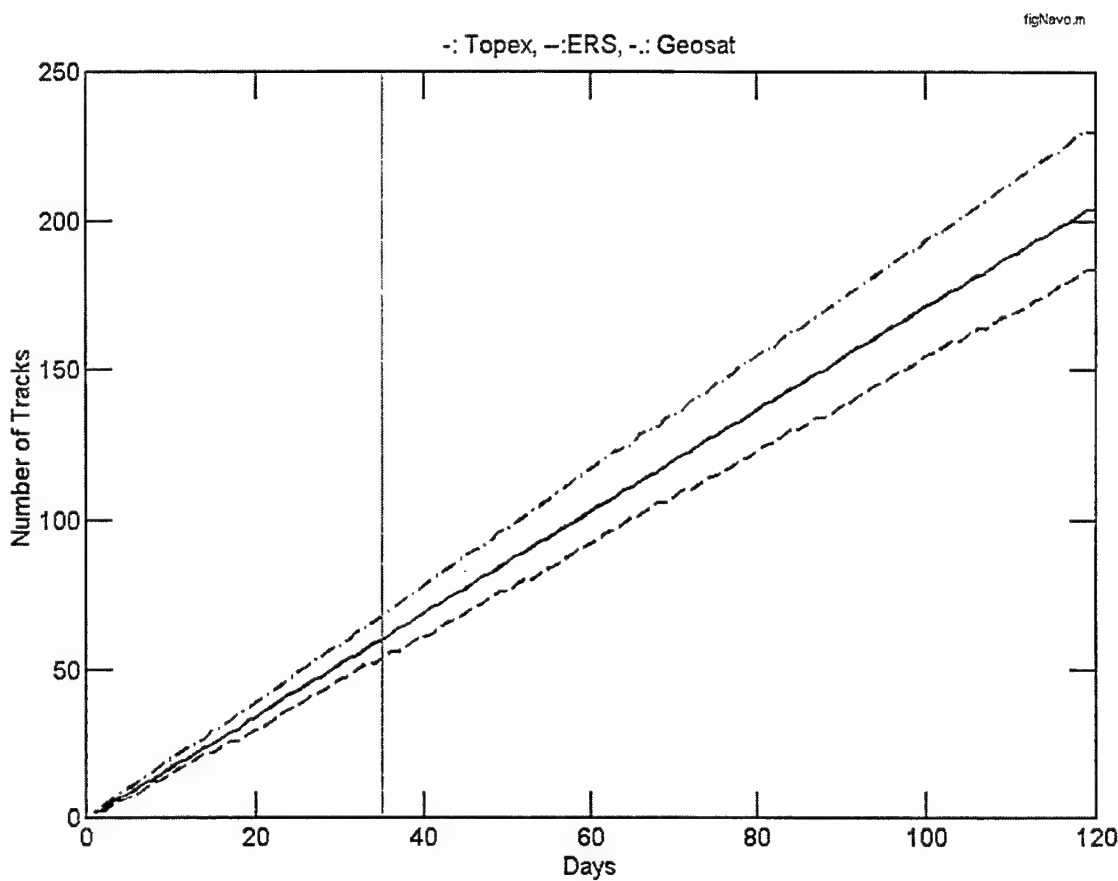


Figure 6. Number of ground tracks in the Yellow and East China Seas region, counting repeated tracks, as a function of time. TOPEX, ERS, and Geosat tracks are denoted by solid, dashed, and dashed-and-dotted lines, respectively.

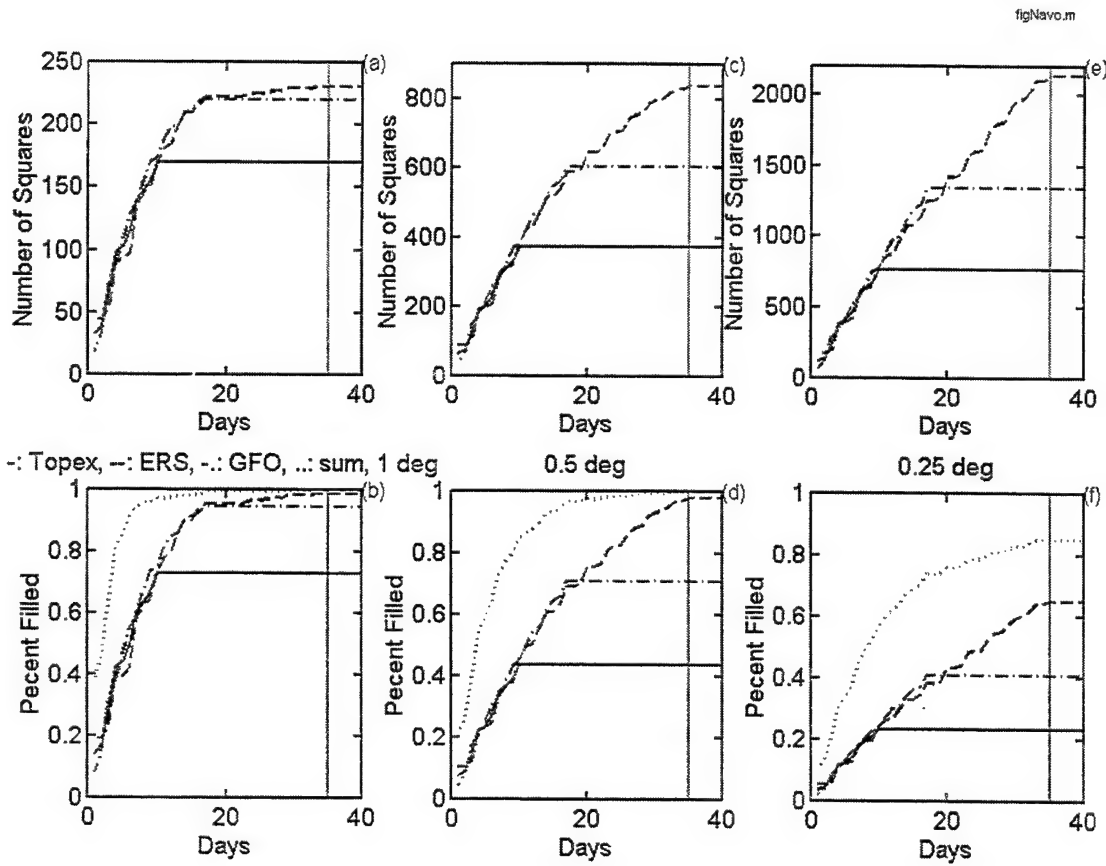


Figure 7. (a) Number of one-degree squares hit by TOPEX, ERS, and Geosat over 40 days. TOPEX, ERS, and Geosat tracks are denoted by solid, dashed, and dashed-and-dotted lines, respectively. (b) Percentage of one-degree squares hit in the Yellow and East China Seas region by TOPEX (solid), ERS (dashed), Geosat (dashed-and-dotted), and combined (dotted) tracks over a 40 day period. (c, d) Same as in (a, b) but for half degree squares. (e, f) Same as in (a, b) but for quarter degree squares.

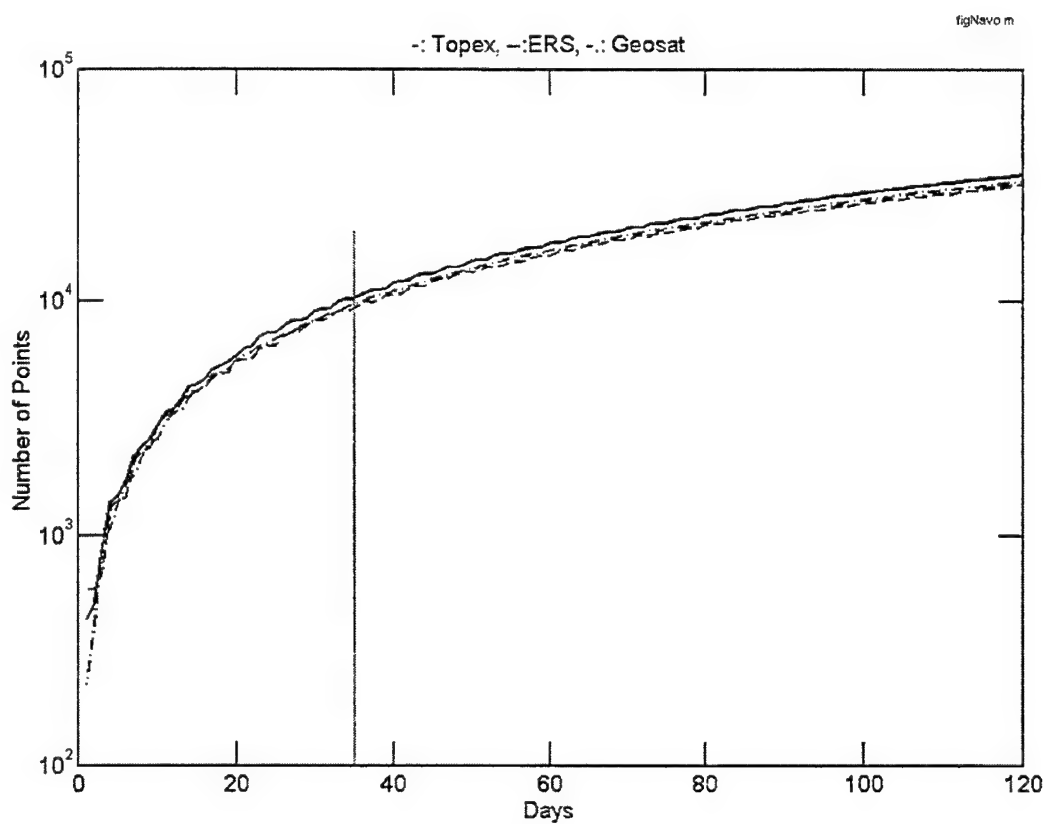


Figure 8. Number of ground points in the Yellow and East China Seas region for TOPEX (solid), ERS (dashed), and Geosat (dashed-and-dotted) over a 35-day period.

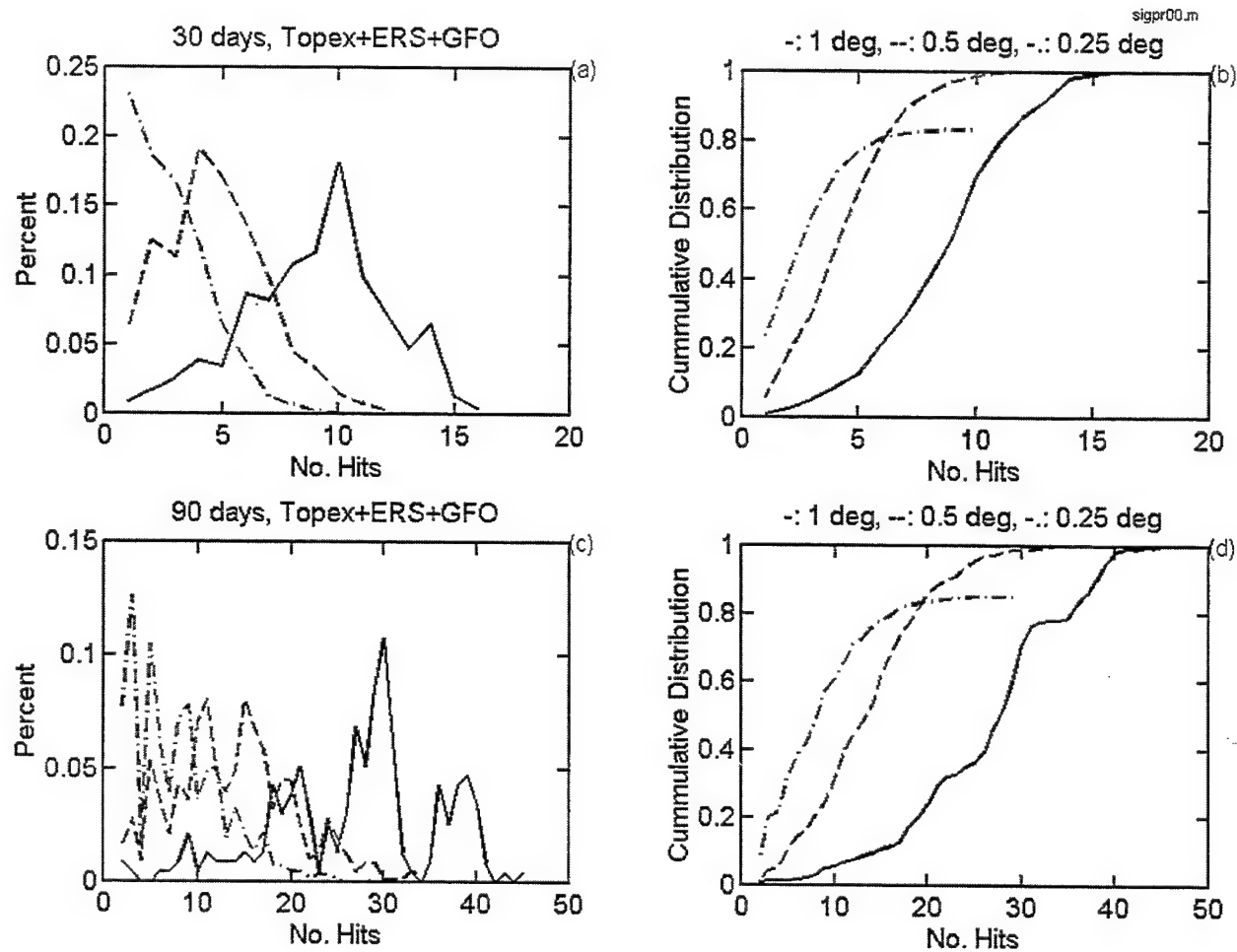


Figure 9. (a) Histograms, and (b) cumulative distributions of number of ground track hits for combined TOPEX, ERS, and Geosat tracks over a 30-day period for one-degree (solid), half degree (dashed), and quarter degree (dashed-and-dotted) squares. (c, d) same as (a, b) but for a 90-day period.

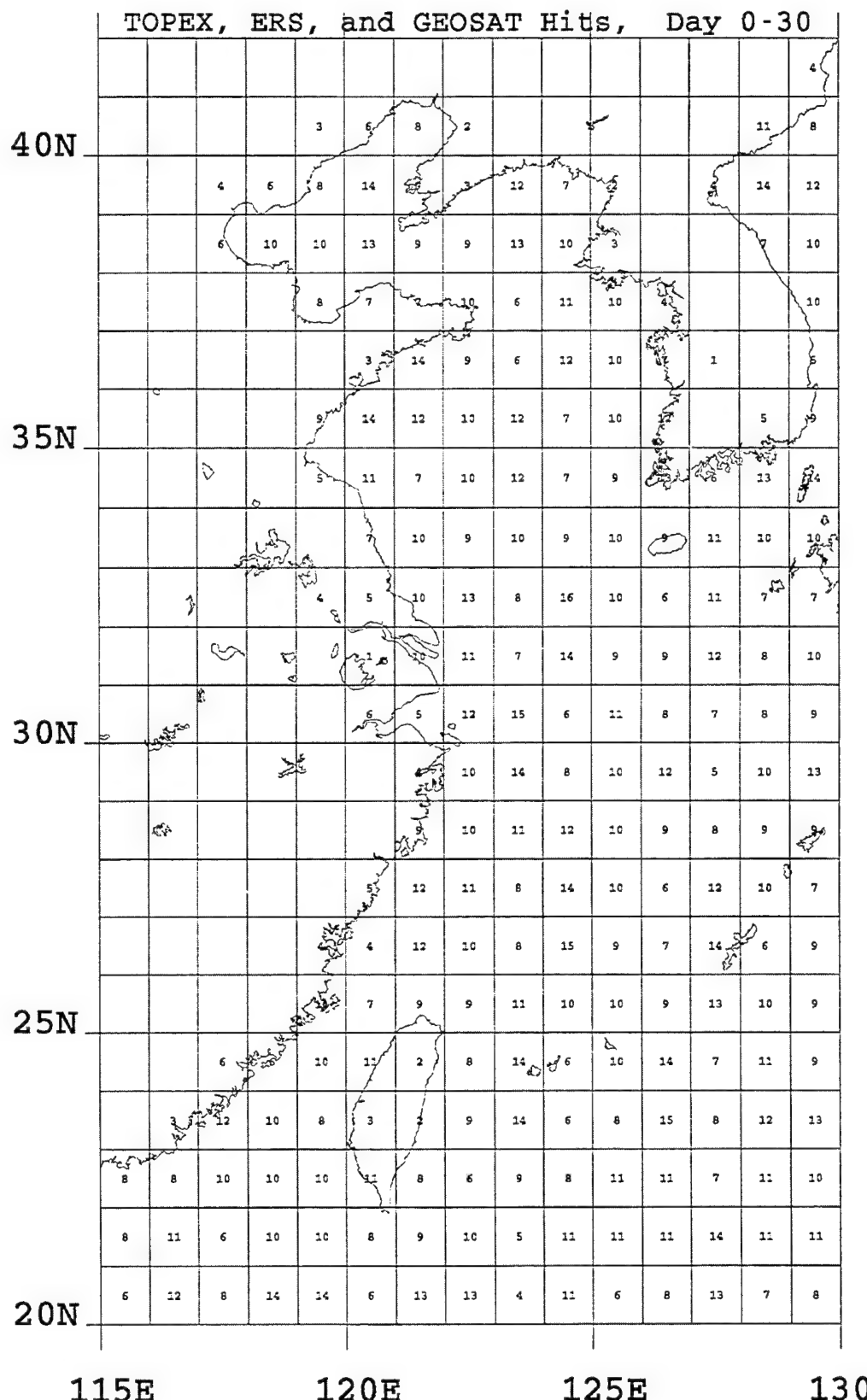
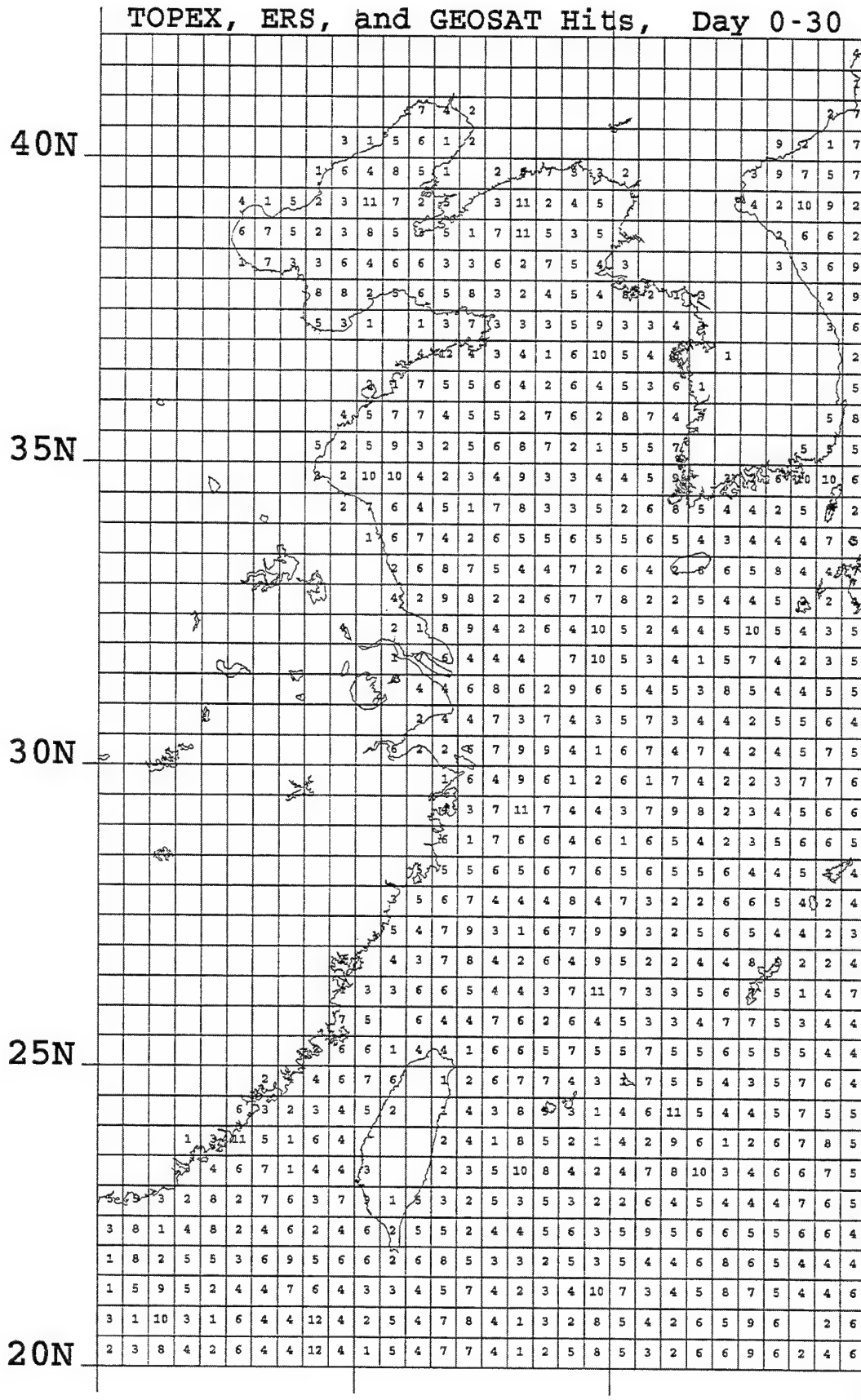


Figure 10. Distribution of combined TOPEX, Geosat, and ERS ground track hits for days 0-30, (a) one-degree squares.

TOPEX, ERS, and GEOSAT Hits, Day 0-30



115E

120E

125E

130E

Figure 10b. half degree squares

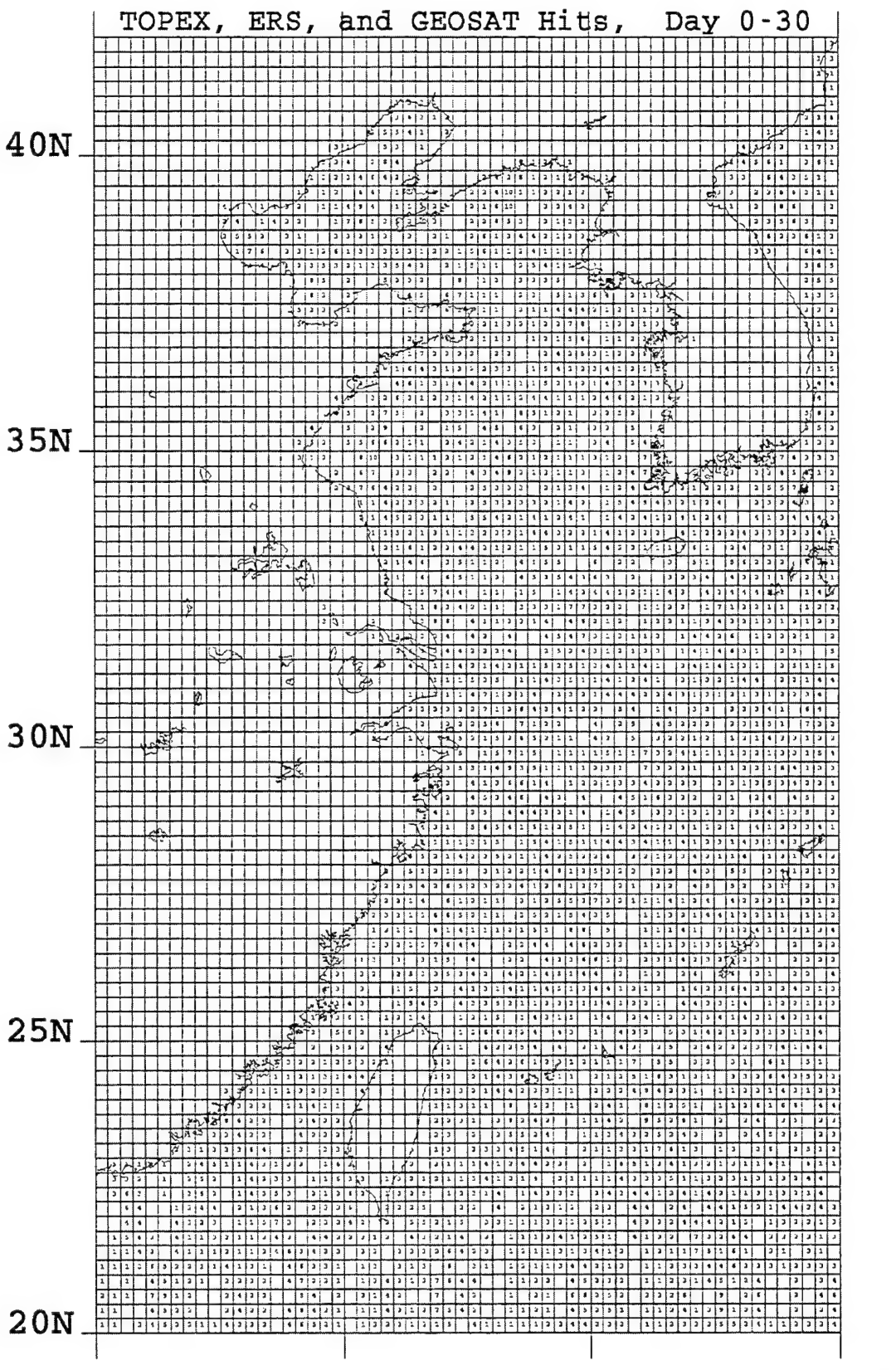


Figure 10c. quarter degree squares

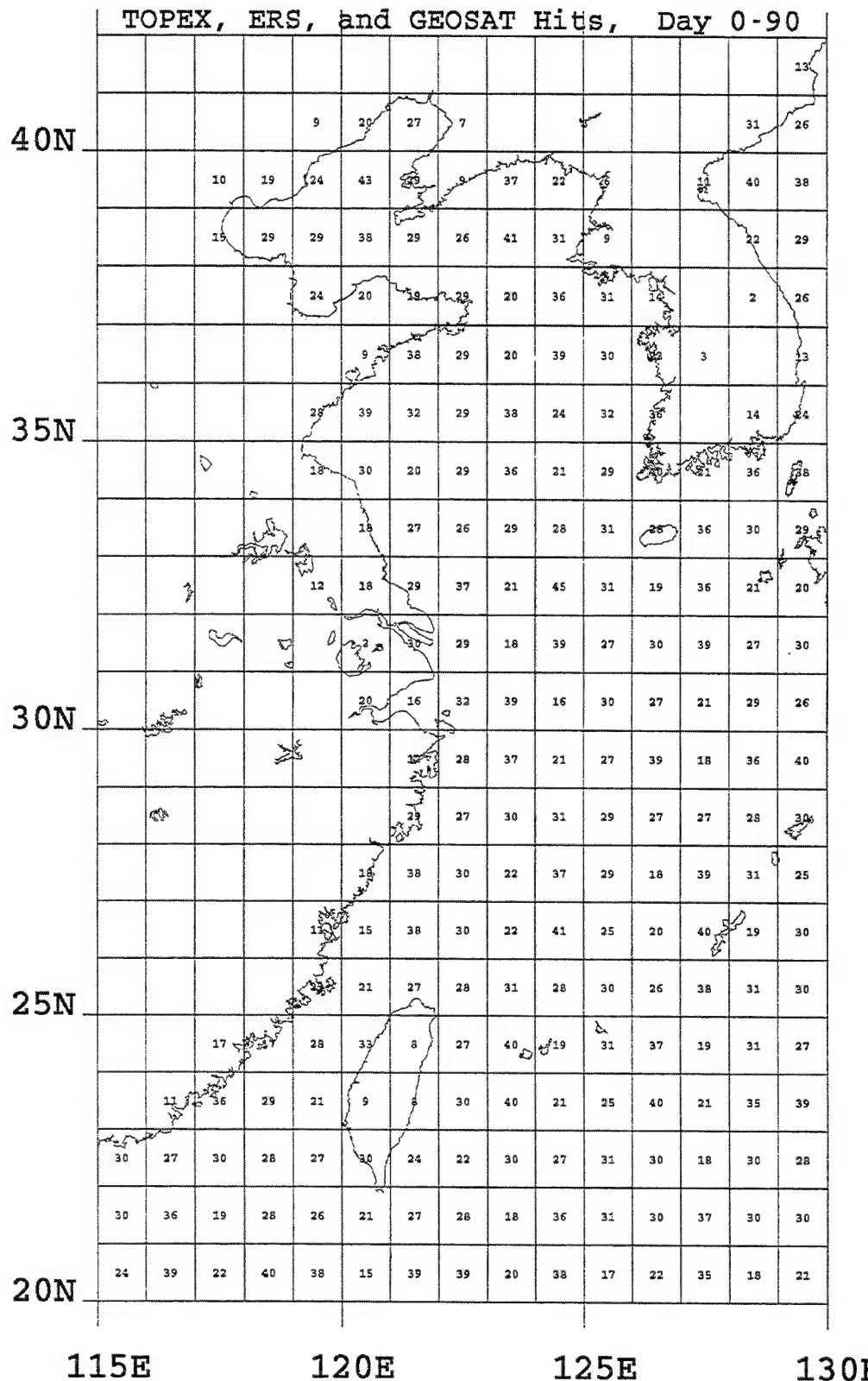


Figure 11. Distribution of combined TOPEX, Geosat, and ERS ground track hits for days 0-90, (a) one-degree squares, (b) half degree squares, and (c) quarter degree squares.

TOPEX, ERS, and GEOSAT Hits, Day 0-90

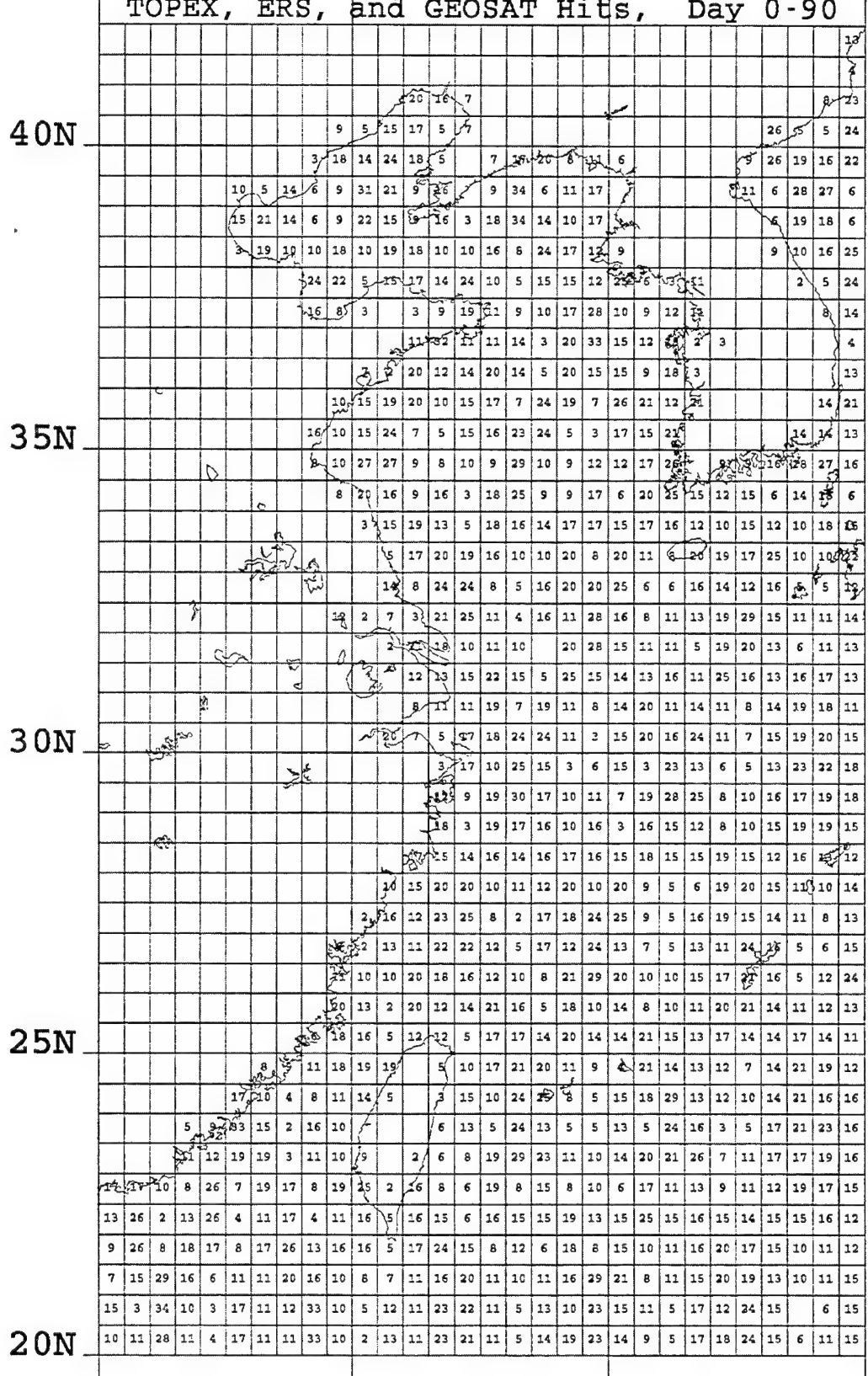


Figure 11b half degree squares.

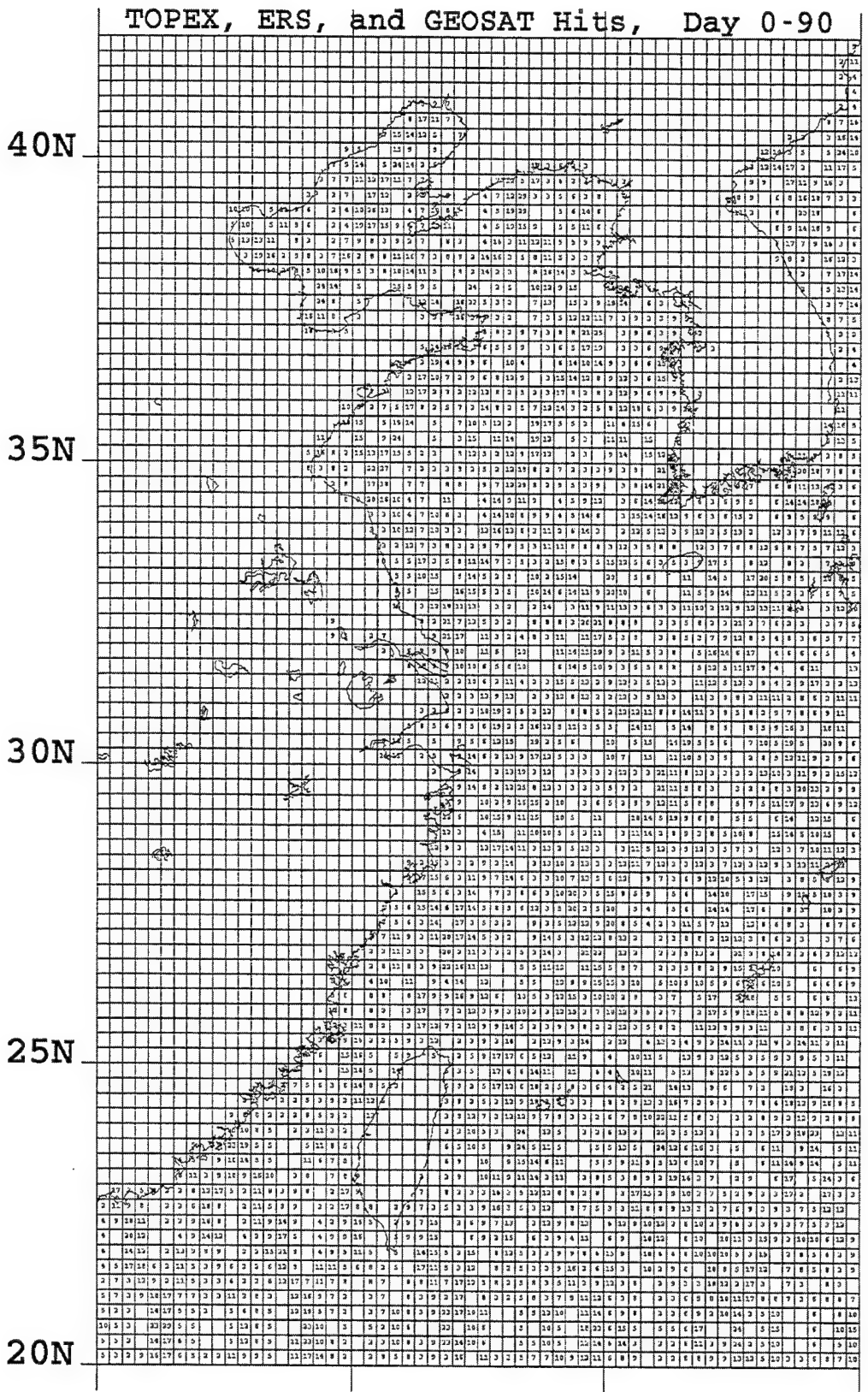


Figure 11c quarter degree squares.

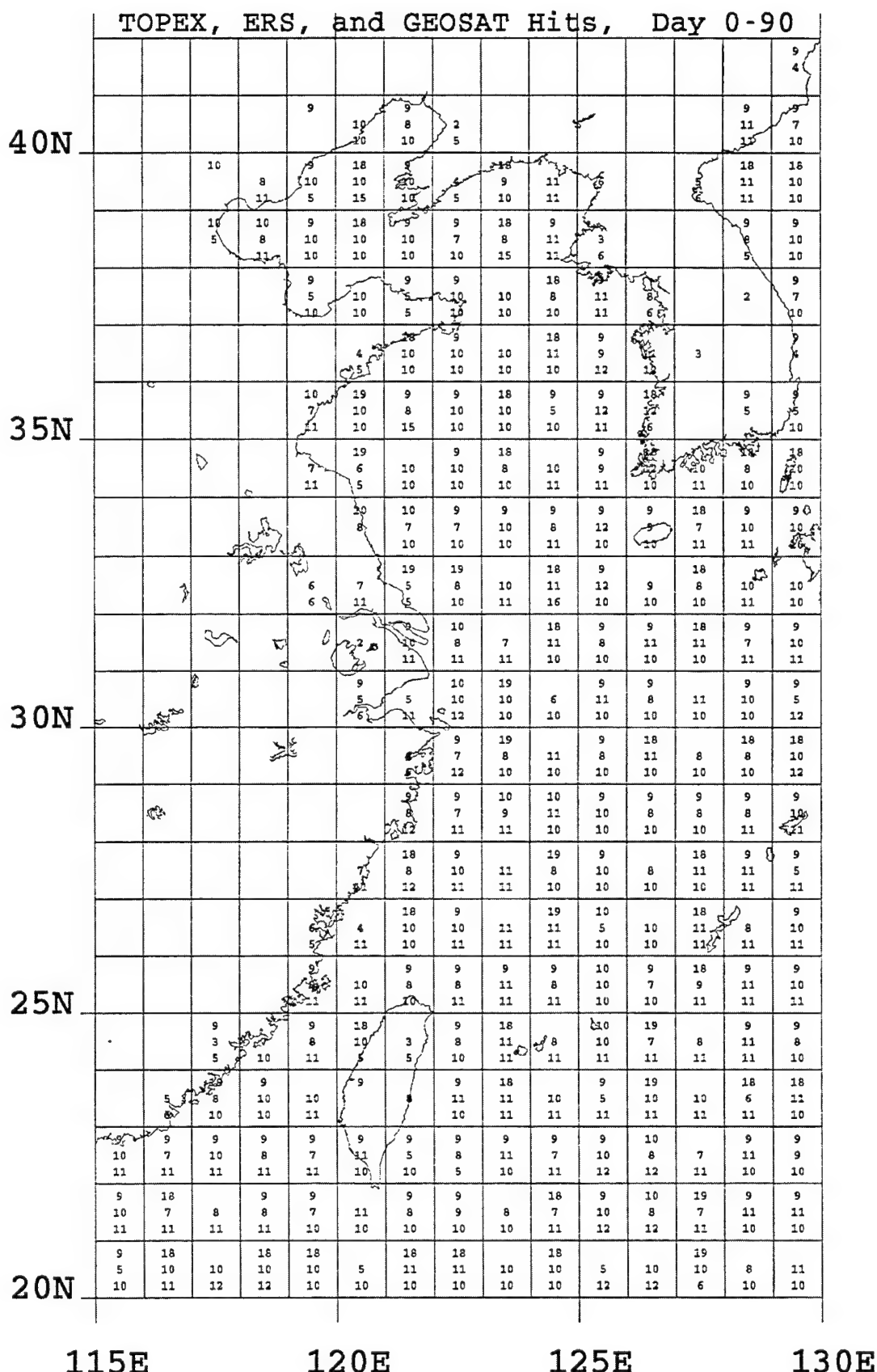
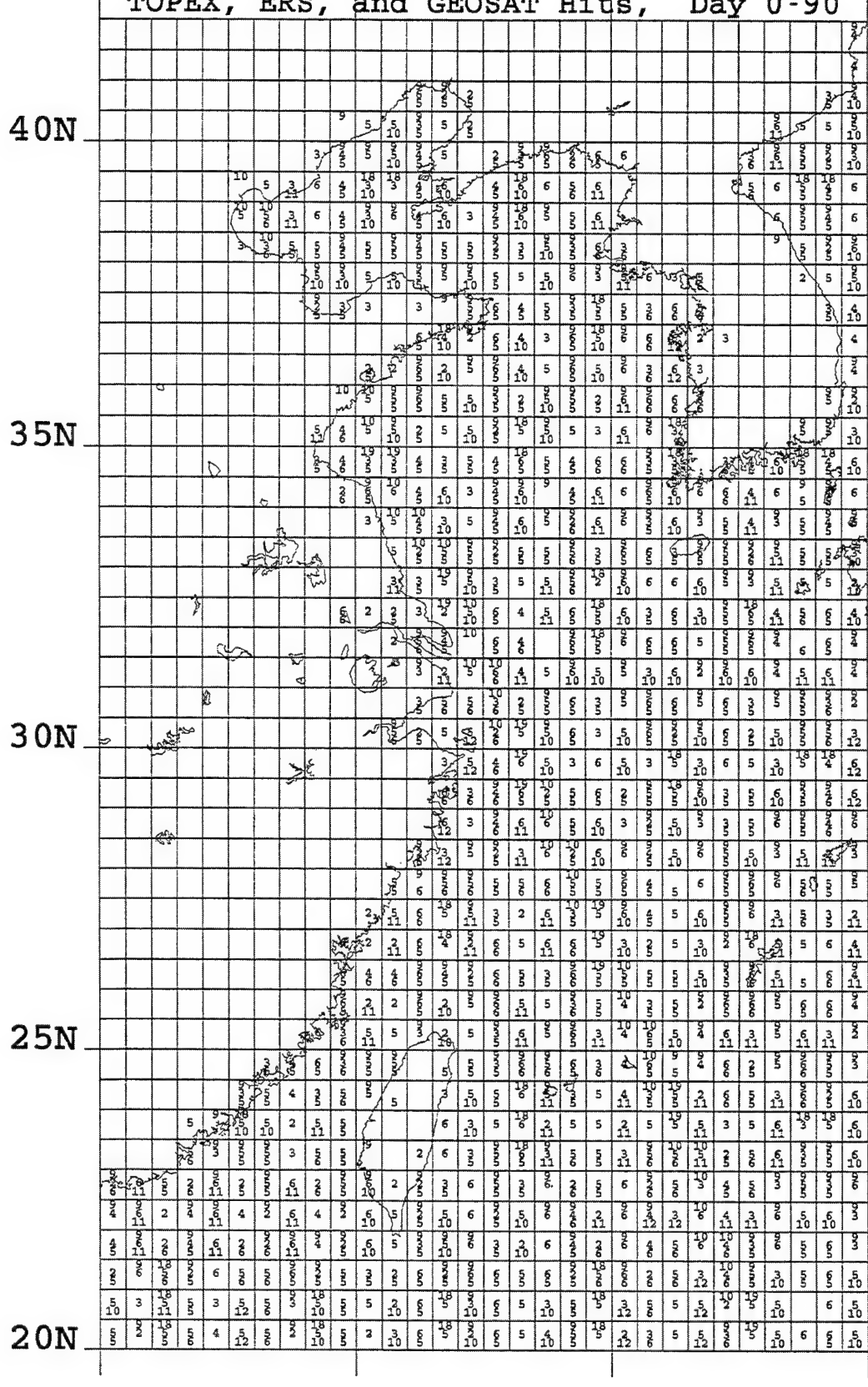


Figure 12. Distribution of individual TOPEX, Geosat, and ERS ground track hits for days 0-90, (a) one-degree squares, (b) half degree squares, and (c) quarter degree squares. Counts in each square reflect TOPEX, ERS, and Geosat from top, middle, and bottom, respectively.

TOPEX, ERS, and GEOSAT Hits, Day 0-90



115E 120E 125E 130E

Figure 12b. half degree squares.

TOPEX, ERS, and GEOSAT Hits, Day 0-90

40N

35N

30N

25N

20N

115E

120E

125E

130E

Figure 12c. quarter degree squares.

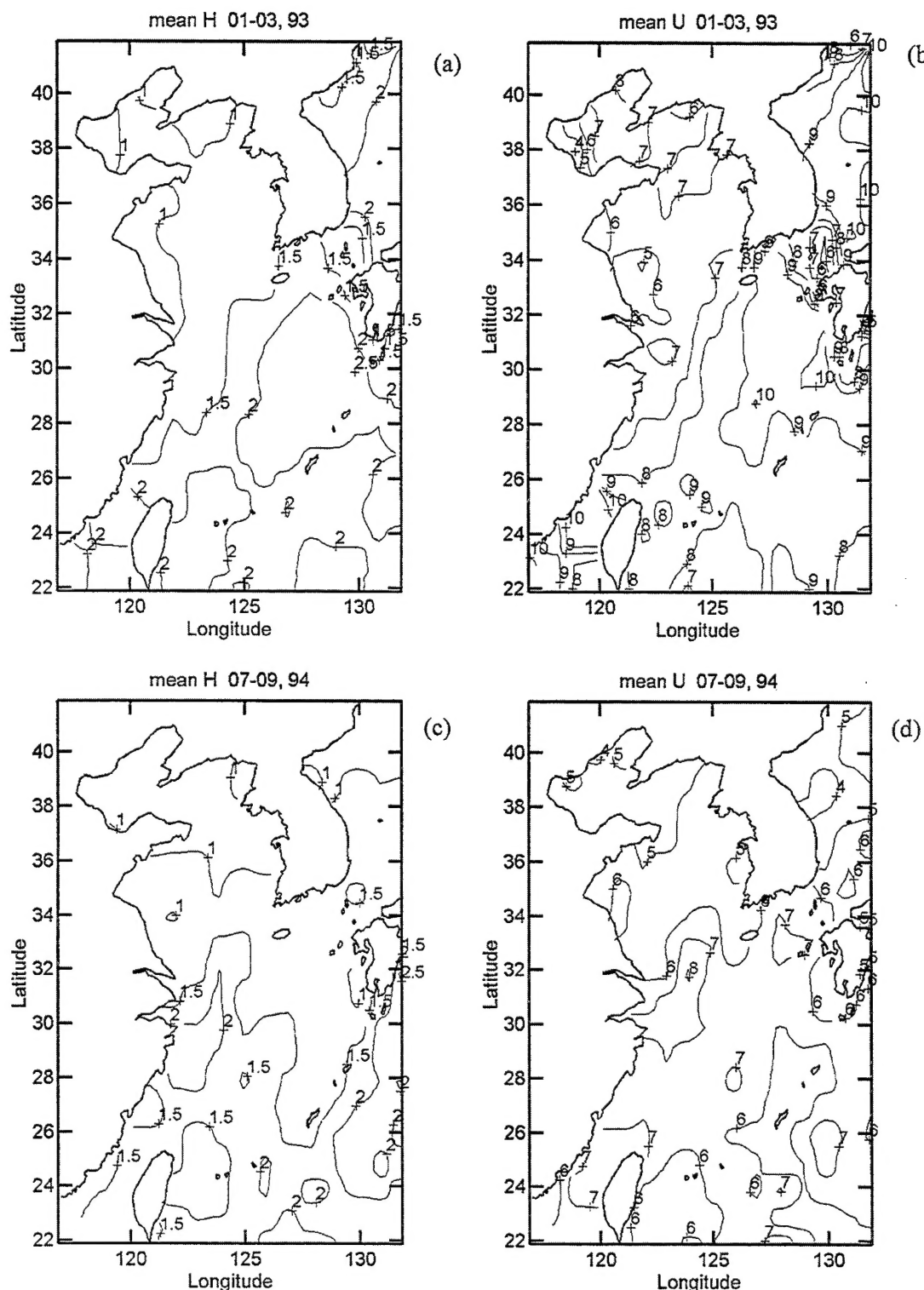


Figure 13. The seasonal climatology of winds and waves in the Yellow and East China Seas. Winter 1993: (a) H_s , (b) U_{10} ; Summer 1994: (c) H_s , (d) U_{10} .

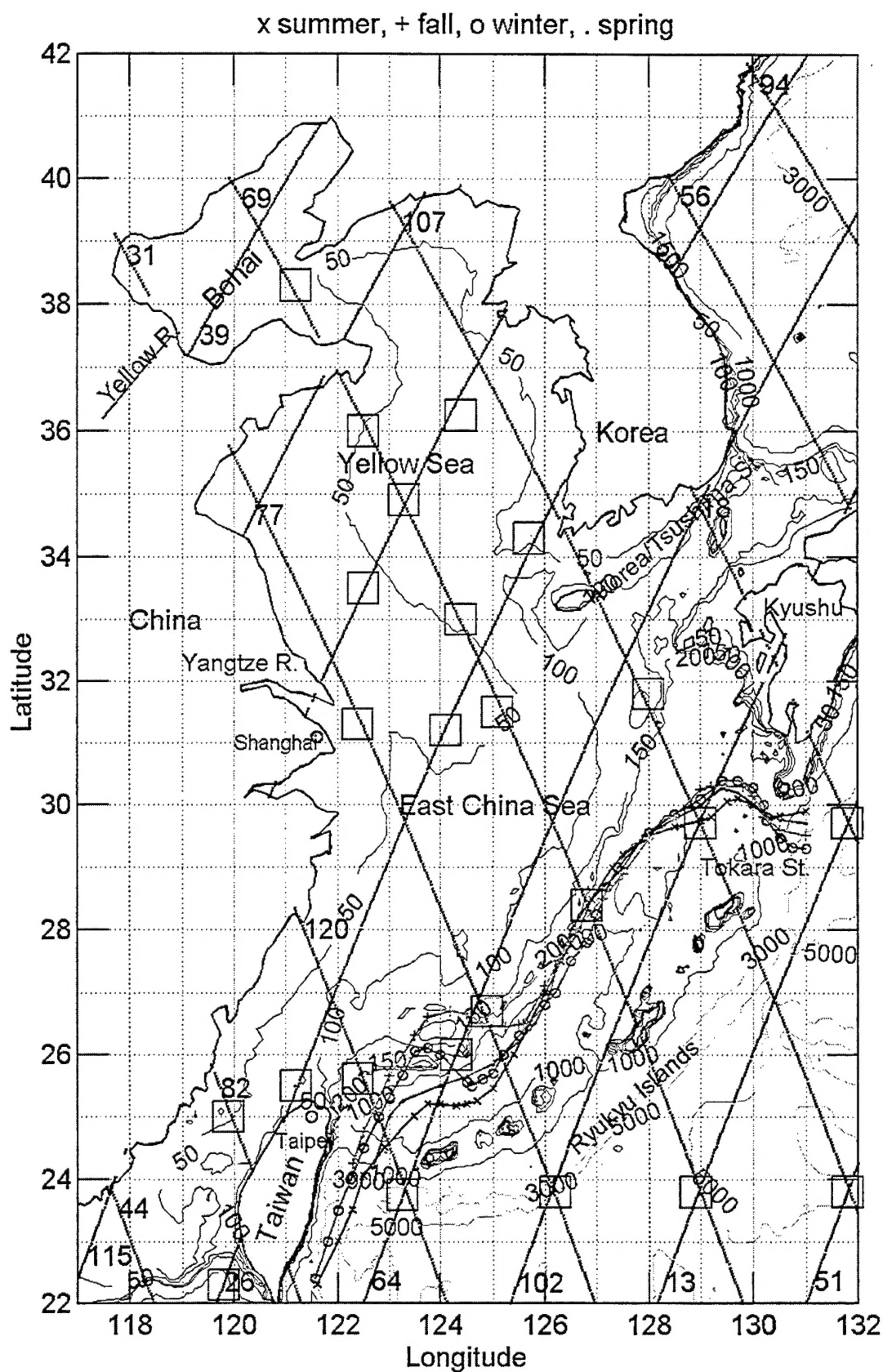


Figure 14. TOPEX ground tracks in the Yellow and East China Seas region and the local bathymetry. The seasonal averages of the Kuroshio axes are superimposed. Squares indicate the locations where the correlation of wind speeds and wave heights are investigated and partially plotted in Figure 15.

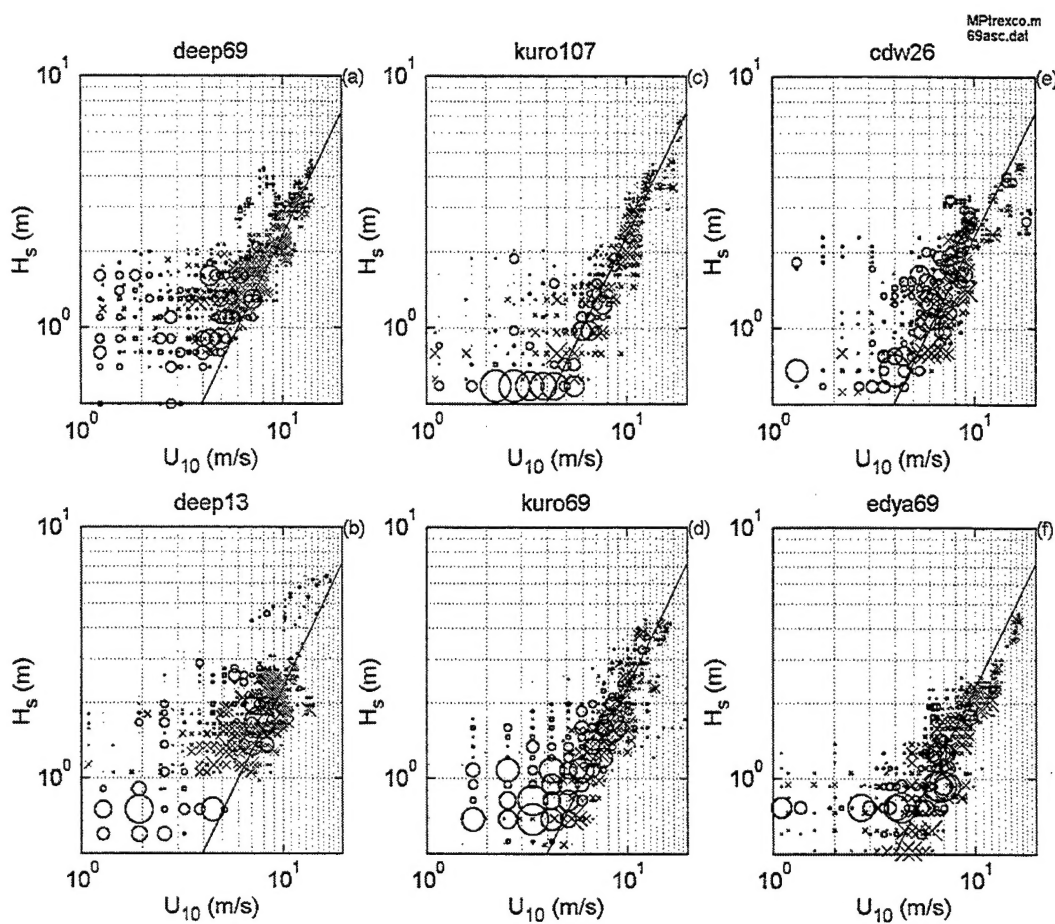


Figure 15. The scatter plots of H_s versus U_{10} several regions of the Yellow and East China Seas. (a) and (b) in deep water south of the Ryukyu Islands; (c) and (d) in the Kuroshio; and (e) and (f), in the middle of East China Sea and Yellow Sea.

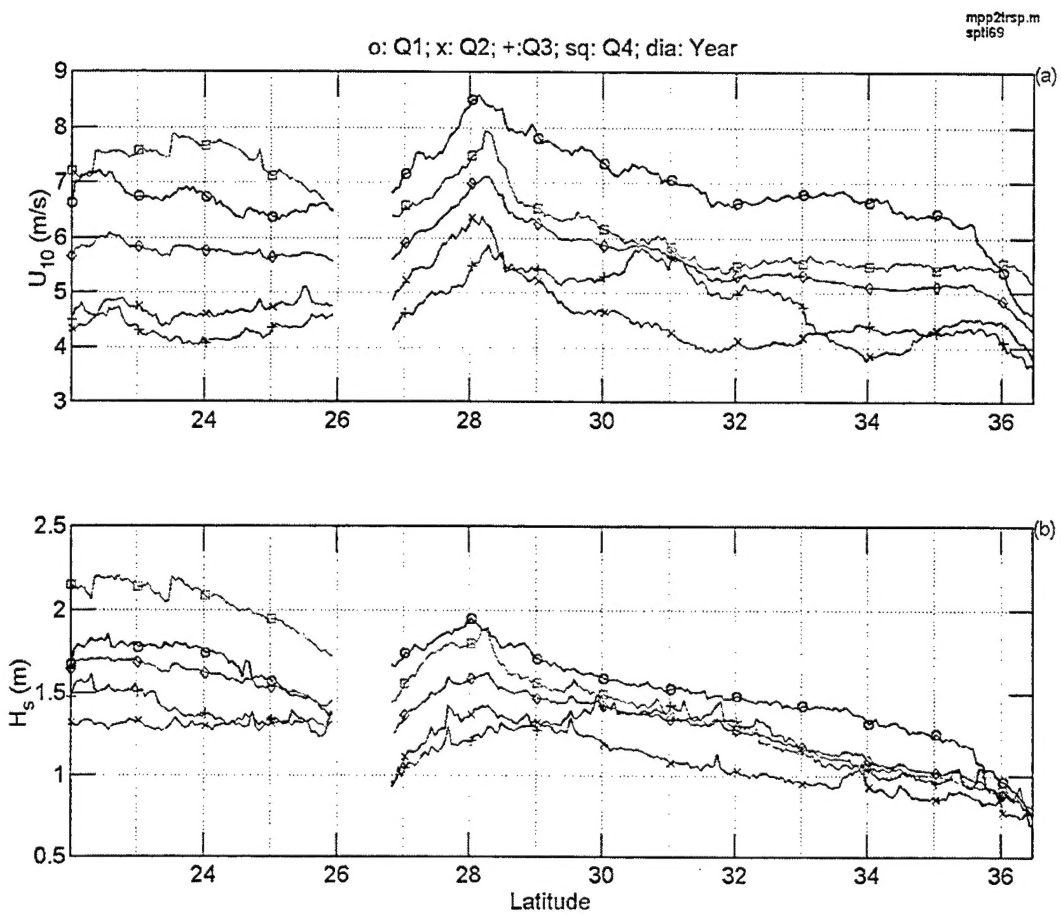


Figure 16. ensemble averages of (a) wind speed, and (b) wave height distributions along groundtrack 69 in the Yellow and East China Seas region. The results are based on averaging four years (1993-1997) of TOPEX output. o: quarter 1, x: quarter 2, +: quarter 3, \square : quarter 4, \diamond : annual average.